Wireless Heating of Resonant Stent with Micro Circuit Breaker for Self-Regulated Endovascular Hyperthermia Treatment

by

Jiaxu Chen

B.Eng., University of Shanghai for Science and Technology, 2016

A THESIS SUBMITTED IN PARTIAL FULFILLMENT OF

THE REQUIREMENTS FOR THE DEGREE OF

MASTER OF APPLIED SCIENCE

in

THE FACULTY OF GRADUATE AND POSTDOCTORAL STUDIES

(Biomedical Engineering)

THE UNIVERSITY OF BRITISH COLUMBIA

(Vancouver)

April 2019

The following individuals certify that they have read, and recommend to the Faculty of Graduate and Postdoctoral Studies for acceptance, a thesis/dissertation entitled:

Wireless Heating of Resonant Stent with Micro Circuit Breaker for Self-Regulated Endovascular Hyperthermia Treatment

submitted by Jiaxu Chen in partial fulfillment of the requirements for

the degree of Master of Applied Science

in Biomedical Engineering

Examining Committee:

Dr. Kenichi Takahata
Supervisor

Dr. Hongshen Ma
Supervisory Committee Member

Dr. Edmond Cretu
Supervisory Committee Member

Abstract

In-stent restenosis remains the most common complication in stent implantation. Hyperthermia treatment through moderate heating of implanted stent is expected to be an effective treatment for restenosis. Toward this goal, this thesis presents a wirelessly powered resonant-heating stent device, with a focus on design improvement, experimental analysis of power transfer and electrothermal behavior, as well as safeguarded thermal regulation of the proposed device.

The stent device, configured to form a passive resonator with a capacitor-integrated inductive stent, was coated with optimized layers of gold and Parylene C to improve the quality factor and heating performance of the device. Wireless testing results of the device deployed in artificial artery has shown its promising thermal performance in physiological saline with a flow rate relevant to stenotic blood flow, while revealing clear merits of resonant-based heating with up to ~220 and ~40 times higher heating rates than off-the-resonance conditions in air and saline flow, respectively. The wireless heating efficiency, as well as the effects of saline temperature and flow rate on the device performance along with other parameters are also studied in details based on the results.

Finally, for the temperature regulation of the stent device, a thermal-sensitive MEMS circuit breaker (1900 × 700 × 605 μm^3) with the function of a power switch is presented. The circuit breaker is fabricated using Nitinol shape memory alloy as a micro-actuator to have a cantilever beam that forms a closed power switch at low temperatures and open switch when the temperature reaches 65 - 69 °C. After integrated with the stent device, the circuit breaker chip is able to open or close the resonant circuit to prevent the stent device from overheating. The intended

functionality of the circuit breaker has been verified from the electrothermal and thermomechanical behavior of the circuit breaker measured in this study. Preliminary experimental results in the wireless heating of the stent device with circuit breaker also indicate that the circuit breaker is capable of limiting the device temperature to be below the threshold.

Lay Summary

The main goals of this research are to 1) design a resonant stent device with optimized stent quality factor for wireless heating in hyperthermia treatment against in-stent restenosis; 2) investigate on the heating performance of the proposed stent device in air and saline used as a substitute solution of stenotic human blood; 3) present a MEMS circuit breaker which is more miniature in size and smaller in resistance for the purpose of temperature control of the resonant stent device in wireless heating. This work will pave the path to further design optimization and performance improvement for resonant stent device with a circuit breaker for heat regulation towards its application to clinical wireless hyperthermia treatment of in-stent restenosis.

Preface

This work is accomplished under the supervision of Professor Kenichi Takahata in Takahata lab at the University of British Columbia. All my individual work throughout my master's research are included in this thesis, in which a resonant stent system and a novel MEMS circuit breaker chip are proposed and analyzed with regards to their physical characteristics and thermal behaviors. I have contributed to the following papers as the first author. The 1st paper cover the contents in Chapter 2 and the 2nd paper cover the contents in Chapter 3. All of the work in this thesis and also two publications below including device and experiment design, as well as the data analysis were conducted by me with the guidance of Professor Kenichi Takahata and also help from Dr. Yi and Madeshwaran Selvaraj.

J. Chen, Y. Yi, M. Selvaraj, K. Takahata, "Experimental Study on Wireless Heating of Resonant Stent for Hyperthermia Treatment of In-Stent Restenosis," submitted to a peer reviewed journal, minor revision requested, under review.

J. Chen, et al. "(tentative title) A MEMS Circuit Breaker for Safeguarded Thermal Regulation in Stent Hyperthermia Treatment," to be submitted to a peer reviewed journal.

The following papers are also what I contributed as a co-author to Dr. Yi's research in our lab during my master's research. While Dr. Yi was responsible for most of his work, I contributed to part of the device and experimental design, and collaborated with Dr. Yi in conducting most of the experiments discussed in these papers.

Y. Yi, J. Chen, K. Takahata, "Wirelessly Powered Resonant-Heating Stent System: Design, Prototyping and Optimization," submitted to a peer reviewed journal, revision requested, under revision.

Y. Yi, J. Chen, M. Selvaraj, Y. Hsiang and K. Takahata, "Wireless Hyperthermia Stent System for Restenosis Treatment and Testing with Swine Model," submitted to a peer reviewed journal, revision requested, under revision.

Table of Contents

List of Tables

List of Figures

Acknowledgements

First, I would like to thank Professor Kenichi Takahata for his valuable and helpful supervision, guidance and support throughout my master's degree and research work in two years. I am very grateful to be able to work and accomplish my research in his lab.

I offer my enduring gratitude to all the faculty, staff members and my fellow students at UBC, who have inspired me to continue my work in this field. I also would like to take this opportunity here to give my sincere thanks to Dr. Mario Beaudoin and Dr. Andrey Blednov at AMPEL Advanced Nanofabrication Facility for their kind help and support in my usage of the cleanroom equipment, as well as Dr. Edmond Cretu for his generous permission for me to use the laser micromachining system.

Special thanks are owed to my parents, whose have supported me throughout my years of education, both morally and financially.

Dedication

Dedicated to my beloved parents and partner Yuxiang Lei

Chapter 1: Introduction

1.1 In-stent restenosis: background, causes and treatments

1.1.1 A brief introduction of cardiac stent implantation and its complication: in-stent restenosis

Cardiovascular disease (CVD) is the major cause of disability and death among adults worldwide [1], with the 2013 Global Burden of Disease (GBD) study estimating that CVD caused 17.3 million deaths globally [2]. Cardiac stent implantation for percutaneous coronary intervention (PCI) against coronary artery disease has grown quickly over past two decades. Since the first approval by the US Federal Drug Administration (FDA) in 1994 against coronary artery disease, bare metal stent (BMS) technology has gained great development and been made available for being delivered into narrowed arteries against artery closure. In spite of its effectiveness in preventing the artery closure, BMS is limited by in-stent restenosis that it brings with [3]. In-stent restenosis is defined as the recurrence of abnormal narrowing of arteries caused by vascular injuries after stent implantation. Incorrect positioning and expansion of stents inside artery, as well as improper stent length and diameter are all risk factors of in-stent restenosis. The prevalence of restenosis is considerably high [4] (e.g., up to ~40% among patients receiving bare metal stent [5]) due to the large amount of population receiving stent implantation to deal with vessel disease, such as stenotic artery or blood blockage. BMS implantation used to be the leading therapy until the application of drug-eluting stents (DES) in 2004 in response to high occurrence rate of in-stent restenosis with BMS [6]. Although drug-eluting stent (DES) has been found to be effective in preventing restenosis with occurrence rate of only ~5% [7], DES therapy has been associated with increased risk of late thrombosis that can lead to heart attacks [8].

1.1.2 Pathophysiology of in-stent restenosis

Figure 1.1 [9] is an integrated view of vascular reactions underlying in-stent restenosis after stent implantation. As can be seen from the figure, the immediate reactions after a stent is implanted into a diseased stenotic artery are mainly denudation of endothelium and aggregation of platelets in close proximity to the stenting site, followed by the leukocyte recruitment (a central immunological process involving the migration of leukocytes across the platelet-fibrin layer into inflammation and injury tissue activated by chemokines released from macrophages), and the release of cytokines (which are crucial in the immune system to fight off infections and can regulate the maturation, growth, and responsiveness of particular cell populations) [9]. Afterwards the cellular proliferation takes place, involving the smooth muscle cells (SMCs) proliferation and migration stimulated by growth factors produced from platelets, leukocytes and SMCs, which seldom happens in normal conditions. The cellular division within the neointima growth occurring at this stage is considered to be essential to the subsequent restenosis occurrence [10]. Over time the cellular reactions reduce while the production of extracellular matrix (ECM) begins to increase, resulting in an artery remodeling process, then the reendothelialization occurs.

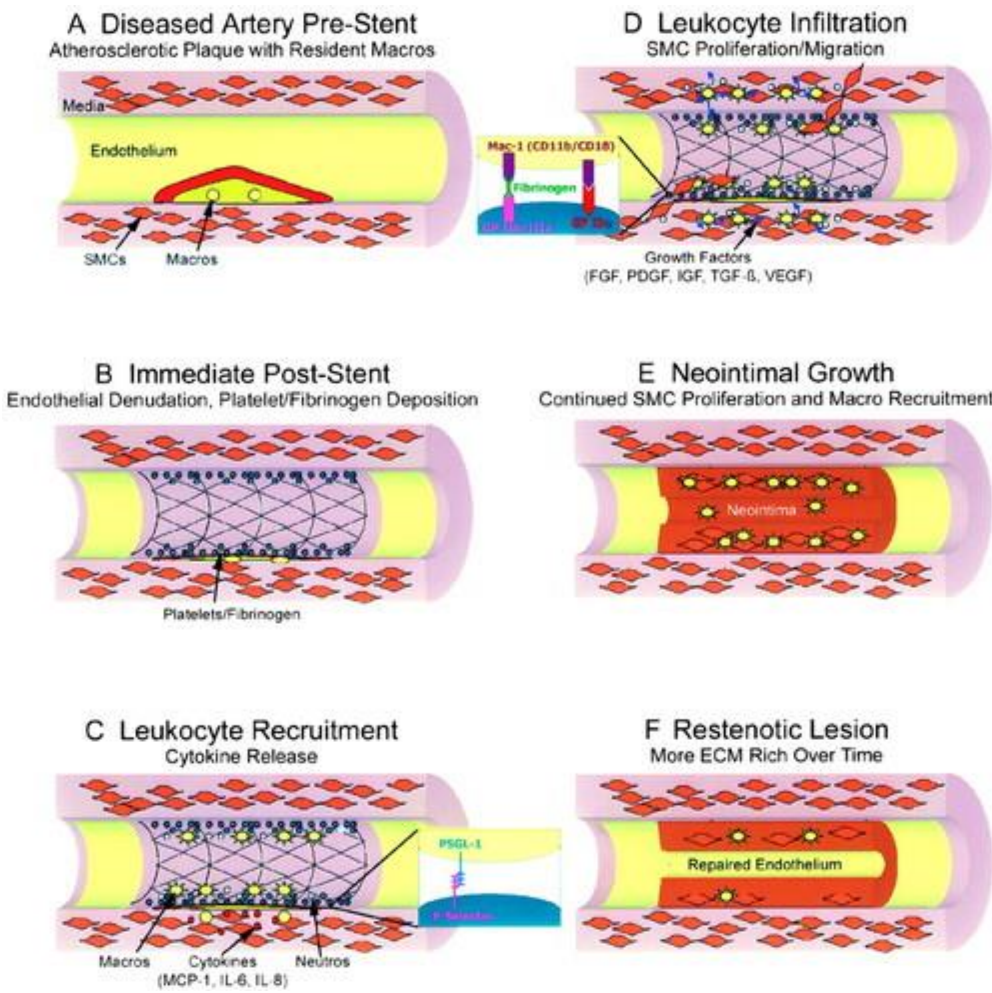

Figure 1.1: An illustration of restenosis development: (a) Atherosclerotic artery wall before stent implantation; (b) Post-stent endothelial denudation and platelet/fibrinogen deposition; (c) Leukocyte recruitment, and cytokine release; (d) Leukocyte infiltration and SMC proliferation/migration after injury; (e) Intimal hyperplasia caused by neointimal growth; (f) More ECM-rich plaques occur and cell proliferation decreases. (Source: [9] with permission)

Apart from vascular wall injuries and lesions that can lead to inflammatory reactions, infections caused by bacterial and viral pathogens from the implanted stent may also increase the risk of restenosis [11, 12]. In addition, cohort studies indicate that risk factors for in-stent restenosis are also related to patient and clinical characteristics. For instance, scientists and clinicians found that diabetes mellitus could be a risk factor, possibly due to a tendency towards exaggerated intimal hyperplasia existing within diabetes patients [13] and another research indicates that, after eliminating potential confounders including stent materials or geometries and medications, lower measured data of systolic and diastolic blood pressure during percutaneous coronary intervention (PCI) are independently relevant to a lower risk of in-stent restenosis [14], suggesting that uncontrolled hypertension within the stenting process could be a risk factor for restenosis.

1.1.3 Hyperthermia treatment: a novel approach for in-stent restenosis

Common therapy methods for restenosis include pharmacotherapy, brachytherapy and vascular gene therapy, etc. The hyperthermia treatment, which is used as a treatment against cancer cells via raising the temperature of cancerous tissue by several degrees, is also receiving considerable attention recently in treating diseased vessel walls, due to its high efficiency and relatively fewer side effects. In addition, scientists also found that vascular endothelial and cardiac functions of patients with chronic heart failure could be improved via repeated whole-body hyperthermia treatment [15]. The hyperthermia treatment usually targets cancerous tissue or cells using a thermoregulation system involving confined heat source generated with different energy sources, such as radiofrequency (RF), microwave, or ultrasound radiation, to increase the temperature of a specific part of body or organ above its own threshold temperature [16]. Hyperthermia treatment generally consists of three types, local hyperthermia treatment (superficial, intracavital, intraluminal and interstitial), regional hyperthermia treatment (abdominal, pelvic, limbs, etc.) and whole-body hyperthermia treatment [17]. The elevated temperature in a hyperthermia treatment generally ranges from 40 °C to 50 °C and the longer the duration of heating, the more the thermal dose will be induced.

The effectiveness of hyperthermia treatment has been also reported for restenosis treatment [18-21]. For example, K. Orihara et al. [18] have verified the efficacy of hyperthermia treatment at 43 °C for 2 hours in suppressing the proliferation of smooth muscle cells (SMCs) which is the main pathogeny of in-stent restenosis. C. Brasselet et al. [19] have also found in their research that hyperthermia treatment by local heating at 50 °C safely prevented neointimal hyperplasia and in-stent restenosis. As the in-stent restenosis occur at the interface between the implanted stent and the coronary artery, there is a need for localized or targeted heating. Applying targeted heat to inner walls of stented arteries was attempted by heating the stents mainly through two different methods. One was to use a thermal balloon catheter that delivers heat to the implanted stents [22]. This surgical approach is however invasive and unsuitable for repetitive treatments. The other method is direct induction heating of implanted stent using externally applied electromagnetic radiations. While this approach does not require surgical procedures, the heating principle, which relies on eddy currents generated in a stent to heat up, needed extremely high electrical powers and corresponding high-power systems as found in [23, 24], which can lead to hazardous situations and raise safety issues in the treatment. Another noteworthy safety-related concern in the induction heating approach is that there is no safeguarded measure of thermal regulation to prevent the overheating of the stents, as the overheating could lead to in-stent thrombosis (over 70 °C) [19, 25] and cell death (over 50 °C) [26].

1.2 Resonant stent for endo-hyperthermia treatment against restenosis: current progress and limitations

To address these constraints, a resonant "hot stent" device was previously proposed and developed for wireless hyperthermia treatment of restenosis [21]. This electrothermally active stent was comprised of the inductive stent, designed to have an overall helical shape upon balloon deployment to work as an inductor or receiver antenna, and a micro capacitor integrated on the stent to form an inductor-capacitor (LC) resonant tank circuit. The LC-tank stent produced heat only when the device was resonated using a tuned external radiofrequency (RF) electromagnetic field. Thus, the stent device could serve as a frequency-selective wireless heater. The resonance-based heating mechanism enabled not only safe operation of stent heating given its high selectivity on field frequency but also a significantly more power efficient system compared with the induction heating method [20]. Furthermore, the integration of a circuit breaker chip [27], custom developed using micro-electro-mechanical-systems (MEMS) technology, allowed for self-regulation of stent temperature for automatic overheating prevention [28].

While experimental testing performed in these studies showed the feasibility of the resonant-heating stent in air, it still requires in-depth analysis of its electro-thermal behavior, including those under biologically relevant environments involved in the particular vascular applications, towards further improvements in the design and construction of the device as well as of the transmitter side of the hyperthermia system. Moreover, although being effective in temperature control, there are a few limitations existing with the proposed circuit breaker that required further improvement for applications in safeguarded hyperthermia treatment. For example, as a vascular implant, the size of the circuit breaker ($2.0 \times 1.5 \times 0.6$ mm^3) is supposed to be minimized to avoid any blockage to the blood flow. Secondly, the resistance of the circuit breaker needs to be limited as much as possible since, when integrated with the LC heater, the large resistance of the circuit breaker would result in not only lower wireless heating efficiency but also serious power consumption and uneven heat distribution. Moreover, when the size is minimized, the resistance of the circuit breaker would increase as a result of smaller electrical contact area. Thirdly, the microfabrication of the circuit breaker needs to be optimized and reduced in cost. For example, the lithography involved in the copper contact pad fabrication on the bottom titanium lid can be replaced in a low cost and simplified way, and the localized SiO_2 deposition only on the tiny scale cantilever in plasma-enhanced chemical vapor deposition (PECVD) usually requires a mask which is difficult to fabricate and to be aligned well with the cantilever of micron scale and almost no photoresist (PR) mask could survive in the high temperature of the PECVD (250-300 °C) process.

1.3 Objectives and approaches

The aim of this study is to investigate on a resonant LC stent device with a focus on the stent Q factor enhancement, experimental study of heating efficiency and electrothermal behavior, as well as to present a novel MEMS circuit breaker for safeguarded thermal regulation of the stent device. Firstly, this work focuses on the experimental analysis of wireless heating performance of the resonant stent device prototyped for in the current work towards wireless restenosis hyperthermia application. As part of this, heating ability of the device resonated wirelessly is improved by coating a thin layer of gold, a highly conductive, biocompatible, and radiopaque material, to raise the quality (Q) factor of the stent device, which is shown to be highly effective for improving the thermal output. The performance characteristics of the developed device are studied to evaluate wireless heating efficiency while comparing the results with those obtained via wired powering to the device. Physiological saline, which serves as an electrically conductive substitute liquid for human blood in the current study, is used as an ambience of the device to assess its heating behavior both without and with flow of the solution. The measurements also reveal the wireless heating dependences on excitation RF power, filed frequency, spatial orientation of the device with respect to the external antenna, and flow rate of the saline. The effect of ambient temperature on the device performance is also investigated.

In addition, this paper also reports a novel MEMS circuit breaker chip incorporating a micro cantilever switch and a capacitor that can be integrated with an inductive stent to form a LC resonant heater for temperature regulated wireless heating against restenosis. There have been some studies of MEMS-based circuit breakers. For example, a prototype based on nickel thermal actuators on silicon was developed for applications in circuit control [29]. The device is however several millimeters in size that is not applicable for stents. More recently, Kedia et al. have investigated a micro resettable circuit breaker with a coupled thermal bimorph structure [30]. However, the operation temperature involved in this device (80.5 °C) is unsuitable for hyperthermia treatment, and its contact resistance (32 Ω - 35 Ω) is too large for efficient resonant heating. The MEMS circuit breaker chip investigated in the current work is micromachined to be highly miniaturized in size (1900 × 700 × 605 μm^3) and improved by reducing its larger resistance resulting from smaller chip size and optimizing its microfabrication in a more achievable and low-cost manner. The circuit breaker chip is also designed to incorporate a micro capacitor layer. The integration of the micro capacitor within the chip contributes to the miniaturization of overall stent device while easing the device packaging. Particularly in this study, a LC stent device comprising of a gold coated inductive stent with enhanced quality (Q) factor integrated with novel circuit breaker chip is proposed and investigated on its feasibility towards applications in wireless hyperthermia treatment. The thermomechanical and electrothermal characteristics of the circuit breaker, as well as the electrical properties of the stand-alone components of the LC stent device were studied and analyzed in this work. In terms of the thermal characteristics of the integrated LC stent device, wireless heating experiments were conducted to investigate on the temperature regulation of the circuit breaker chip and the heating performance of the whole stent device in air.

1.4 Thesis outline

Chapter 2 presents a LC resonant-heating stent device integrated with a capacitor that can be wirelessly heated for the purpose of application in hyperthermia treatment. Design improvement methods for the quality factor and heating efficiency enhancement are discussed in details. Optimization methods of gold and Parylene C coatings to raise the device's quality factor and heating performance are discussed. Wired and wireless testing results of the stent device in air and saline are analyzed and calculated to evaluate the wireless heating efficiency of the device. The heating performance of the proposed device in physiological saline at body temperature (37 °C) with flow rate relevant to stenotic blood flow is also described.

Chapter 3 introduces a thermal sensitive MEMS circuit breaker for temperature control for safeguard hyperthermia treatment. Design and microfabrication of the MEMS circuit breaker which incorporates a circuit breaker power switch and a capacitor are discussed. The thermomechanical behavior of the circuit breaker as well as the effects of different coating and adhesive materials on the electrothermal characteristics of the circuit breaker are also analyzed and discussed in this chapter. At last, thermal behavior of the LC resonant stent device which consists of a gold coated inductive stent and the proposed circuit breaker chip are analyzed in this chapter.

Chapter 2: Experimental Study on Wireless Heating of a Resonant Stent Device

This work will focus on the experimental study of wireless heating performance of the resonant stent device prototyped towards wireless hyperthermia treatment against restenosis (Figure 2.1). As part of this, heating ability of the device resonated wirelessly is improved by depositing a thin layer of gold, a highly conductive, biocompatible, and radiopaque material, to enhance the quality (Q) factor of the stent, which has been proven in this work to be highly effective for improving the thermal output. The performance characteristics of the developed device are studied to evaluate the wireless heating efficiency while comparing the results with those obtained via wired powering to the device. Physiological saline, which serves as an electrically conductive substitute solution for human blood in the current study, is used as one of the device ambiences to assess its heating behavior both without and with flow of the solution. The measurements also reveal the wireless heating dependences on excitation RF power, field frequency, spatial orientation of the device with respect to the external antenna, and flow rate of the saline. The effect of ambient temperature on the device performance is also investigated.

2.1 Working principles

The thermally active stent investigated in this study works not only as a mechanical scaffold for arteries when implanted, but also as a RF resonant power receiver based on the passive LC tank circuit to produce mild heat being excited by an external electromagnetic field with the same aligned resonant frequency, f_R as the stent device (Figure 2.1 (a)). The transmitter antenna that radiates the field is intended to be placed above the skin below which the active stent device is implanted in the artery. When the LC circuit based resonant device is exposed in an RF electromagnetic field, AC current at the field frequency is generated in the circuit due to the electromotive force (EMF) induced by the field (Figure 2.1 (b)). The power transferred to the device is maximized and converted to Joule heat in the inductor most effectively, when the frequency of the current, or that of the RF magnetic field matches with f_R of the LC circuit, leading to the following condition [31]:

$$\mathrm{P}(f_\mathrm{R}) = \frac{v^2}{R} \tag{1}$$

where v is the EMF, and R is the resistance of the inductor, which is the inductive stent in this study. The steady-state temperature rise, ΔT, in the inductive stent can be described as [31]:

$$\Delta T = \frac{R_T v^2/R}{1+\partial_R R_T v^2/R} \tag{2}$$

where R_T is the thermal resistance of the stent device to the surrounding, and ∂_R is the temperature coefficient of the resistance of the inductive stent. For the hyperthermia treatment of in-stent restenosis, a target level of ΔT (temperature rise above the body temperature in human) may be set at around +6 °C given the reported result [32, 33].

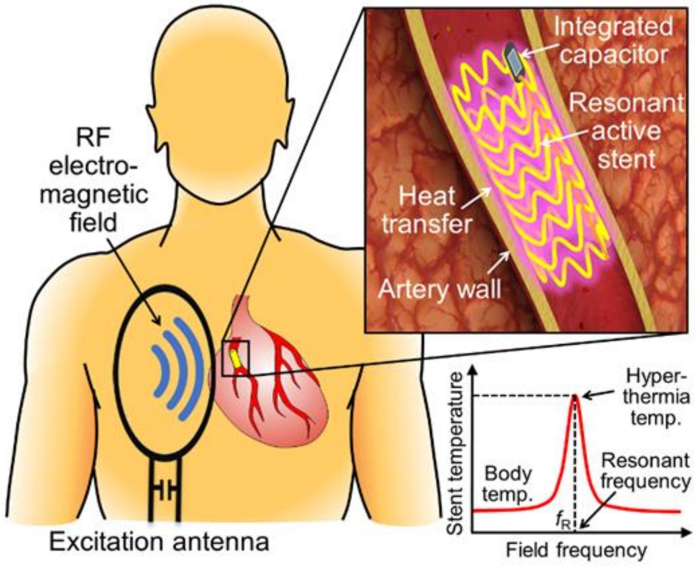

(a)

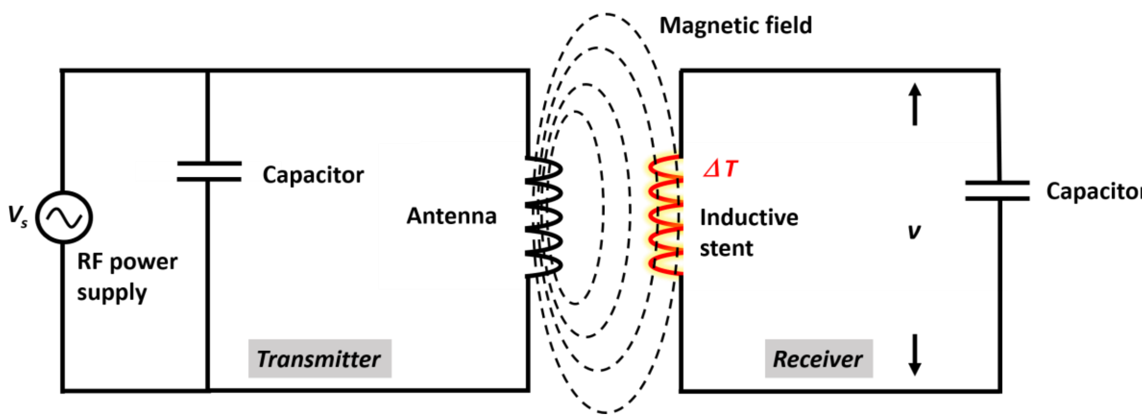

(b)

Figure 2.1: Conceptual schematic of (a) the resonant-heating stent illustrating its target application in wireless endo-hyperthermia for inhibition and treatment of in-stent restenosis; (b) the equivalent circuit showing the wireless heating of the resonant stent device by the excitation antenna.

The inductive stents used in this research are laser micromachined from medical-grade (type 316L) stainless steel tubing [34]. The stent is designed to have a helical pattern as its overall shape that is comprised of 17 zigzag loops (without bridges between the loop), which allows for the stent to radially expand upon the inflation of the balloon catheter on which the stent is mounted, and forms a solenoid-like structure upon expansion so that it serves as a helical inductor of the LC tank. The unexpanded stents are 20-mm long with an outer diameter of 2 mm, 90 ± 10 µm in wall thickness, and 120 ± 10 µm in width of the zigzag wires, and can be expanded up to 6 mm in diameter. A tab-like platform (2.0×0.6 mm^2) is accommodated at each end of the stent body for the integration of a functional chip (capacitor in this study) on the stent. The inductance of the expanded stent (with 6-mm diameter) is measured to be ~ 390 - 430 nH.

The stainless steel, the material of the inductive stent, has a relatively high resistivity, which is not a suitable condition for the stent device to work as an effective LC resonator, as its Q factor is inversely proportional to the resistance of the circuit, which mostly comes from the resistance of the inductive stent. Furthermore, the RF current that flows through the stent is subject to the skin effect, which is the tendency of the AC current to flow through the surface layer of the conductor within a certain thickness (skin depth) that depends on the frequency of the current. It is expected that the AC current flowing in the highly conductive area can help achieve overall reduced stent AC resistance. For this purpose, a highly conductive metal layer is to be deposited on the stent with a thickness greater than the skin depth at f_R of the stent to minimize the AC resistance and thus effectively enhance the Q factor of the device. Gold is selected in this work as the coating material which can provide a ~30 × lower resistivity compared with that of the stainless steel. The skin depth, δ, as a function of frequency, f, is expressed is expressed as [35]:

$$\delta = \sqrt{\frac{2}{2\pi f \mu_0 \sigma}} \tag{3}$$

where μ_0 is the permeability of free space, and σ is the conductivity of the current carrying layer. The skin depth of gold is theoretically ~11 μm at the working (resonant) frequency of the device (that is selected to be 40 - 50 MHz at the expanded state – refer to Section 2.3.1) in this work. Therefore, the gold deposition should be greater than 11 μm for Q-factor enhancement. However, the gold coating thickness should not be too large, as it can lead to not only a need for significantly high balloon pressures to expand the stent, but also a higher chance for peeling of the coated layer upon expansion (due to a higher buckling force that appears in the layer during the expansion). To fulfill these needs, in this study, a 14-μm-thick gold layer is deposited on the inductive stent.

2.2 Prototyping of the resonant stent and transmitter

The gold deposition on the inductive stainless-steel stent was performed using the electroplating process in a similar manner as in [36]. The dependence of deposited thickness on the plating time was characterized to achieve the target thickness of 14 μm on the stent with an adjusted process time (Figure 2.2(a)). The LC-tank stent device was then constructed by integrating with the stent a commercially available thin-film capacitor microchip which has a capacitance of 22 pF and a size of $1.60 \times 0.81 \times 0.73$ mm^3 (0402ZK220GBWTR, AVX Co., SC, USA). This capacitance was chosen to suppress the resonant frequency within the 10 MHz order whose tissue penetration depth was reported to be up to 13 cm [37] sufficient for cardiac applications [38]. Conductive epoxy (CW 2400, Chemtronics, GA, USA) was used to connect one of the capacitor electrodes to the tab platforms of the stent so that the capacitor microchip was electrically coupled with the stent. The other electrode of the capacitor microchip was bonded to the other side of tab platform via thin (38 AWG) copper wire using the same adhesive, completing the LC tank loop with the stent (Figure 2.2 (b)). The resistance that was added by this interconnecting copper wire was negligibly small

(~0.1 Ω). For wired powering/heating tests as well as measurement purposes, a piece of the same copper wire (~5 cm length, ~0.2 Ω resistance) was also bonded to each tab platform to have electrical interface to the device (so that the inductive stent and the capacitor were connected in parallel with the two interfaces). Next, after the LC stent device construction, conformal coating of Parylene C, a proven biocompatible polymer [39], was performed on the entire surface of the device using a commercial system (PDS 2010 Labcoter 2, Specialty Coating Systems, IN, USA). In addition to securing the biocompatibility, this coating also ensured complete electrical insulation of the device from its surrounding (blood and vessel tissue in the target application, both of which are electrically conductive), which was essential to maintain the resonance and resultant heating in the stent.

Finally, the fabricated LC stent device was expanded using a balloon catheter (Advance®35LP Low Profile PTA Balloon Dilatation Catheter, Cook Medical Inc., IN, USA) in 6-mm-diameter silicone-based artificial artery tubes (Dynatek Labs, MO, USA) in order to evaluate the device's resonant heating performance. The stent device mounted on the balloon catheter was inserted into the artificial vessel of 6 cm long and then expanded by hydraulically inflating the balloon with pressure of 15 Atm/Bar using an inflation device (Cook Sphere® Inflation Device, Cook Medical Inc., IN, USA). The stent device was proven to be robust enough with no detectable defect caused in both mechanical and electrical functions after the expansion process.

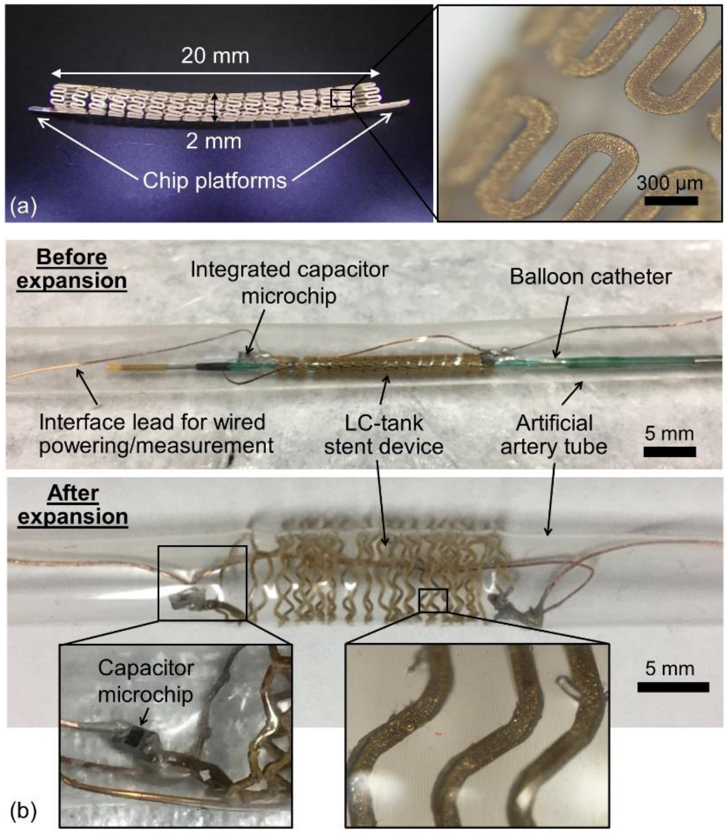

Figure 2.2: Prototyping results: (a) Gold-coated stainless-steel inductive stent at its unexpanded state, with a close-up inset image showing the zig-zag pattern of the expandable tubular body; (b) a LC-tank stent device with an integrated capacitor microchip showing (upper) the pre-expansion device on a deflated balloon catheter positioned inside the 6-mm-diameter artificial artery tube and (lower) the device after balloon expansion (catheter removed) with close-up inset images of the capacitor region and expanded zig-zag wires of the stent.

For the purpose of high power transfer and heating efficiency to the stent device, the wireless link with the external transmitter was configured by the resonance-based wireless power transfer scheme [40, 41], in which the power transmitter (a single loop antenna in this work) was designed to be a same LC resonator as the stent device, with their f_Rs being matched with each other.

Fabricated using thick copper wire (14 AWG) with low resistance, the loop antenna is designed to have a rounded shape of 5 cm in diameter that could provide a symmetric magnetic field for its use as the power transmitter of the system. This loop antenna, measured to have an inductance of 113 nH, was coupled with a discrete capacitor with a selected capacitance to match its f_R with that of the expanded stent device under test. For example, by coupling itself with a capacitor of 101 pF, the f_R of the antenna was tuned to be 47.1 MHz so that this f_R matches that of device #3 (refer to Table 2.2) in air. The antenna can be powered with a RF power amplifier (ZHL-100W-GAN+, Mini-Circuits, NY, USA) connected to a RF signal generator (8657A, Hewlett-Packard Co., CA, USA) to produce an electromagentic field at the specific frequency. The actual input power to the antenna was monitored through antenna's voltage waveforms, as well as current waveforms measured using an AC current probe (CT-1, Tektronix Inc., OR, USA) coupled with the antenna.

2.3 Experimental results and discussions

The electrical and resonant characteristics of the prototyped resonant stent devices were first characterized and analyzed, which reveals the effects of gold and Parylene coatings on the resonance of the device. The resonant heating performances with varying gold and Parylene thicknesses were investigated to select the most power-efficient prototype for further evaluations. Wireless heating characteristics of the selected device, with both vertical and parallel orientations with respect to the excitation antenna, were then studied in three different ambient conditions, i.e., air, saline without flow, and saline with flow at room temperature, and the results were compared with those obtained by wired powering to the same device in order to assess the wireless heating efficiency. The results were also compared with the case under saline flow at body temperature to evaluate the impact of ambient temperature on the device performance.

2.3.1 Electrical characteristics of prototyped device

The electrical characteristics of the inductive stents including its Q factor were measured for varying gold coating conditions, i.e., with no coating, 9.5-μm-thick coating, and 14-μm-thick coating, by connecting each device to an LCR meter (4275A, Hewlett Packard, CA, USA, for resistance and inductance measurements) or a spectrum-impedance analyzer (4396B, Agilent Technologies, CA, USA, for Q-factor measurement) through the bonded interconnecting copper wires. From Table 2.1, which is the summary of the characterized electrical properties, changes in the stent inductance in varying gold coating conditions were observed to be minor. It can be seen that in contrast, the resistance of the stent was significantly lowered with thicker gold coating (within tested thicknesses). The results also showed that the stent's Q factor was raised with gold coating, resulting in an 8.1× improvement with the thickness of 14 μm when compared with the case of no coating. This is a reasonable outome as the Q factor is inversely propotional to the resistance which was effectively lowered by thicker gold deposition.

For the characterization of resonant features, three different LC-tank stents with different thicknesses of gold layer (9.5 μm and 14 μm) and Payelene C layer (8 μm and 30 μm) were prepared as summarized in Table 2.2. Their resonant behavior were wirelessly measured through the impedance phase-dip method as described in [36] using a reader antenna connected with the spectrum-impedance analyzer. All the devices were expanded in the 6-mm-diameter artificial artery, which was filled with either air or saline for the study of their impact on the devices' resonant behavior. The measured results with air and saline surroundings are shown in Figure 2.3 (a-b), respectively. The f_R values of each stent deivce in both air and saline were determined from this measurment (Table 2.2). These values show good match with theoretical ones (51.7 - 54.3 MHz) estimated using the measured inductance value of expanded stent mentioned above with the 22 pF capacitance. The stent of the 1st device has the lowest stent Q factor of 8.2 while the latter two have higher Q factor around 16.6.

	DC resistance (Ω)	Inductance (nH)	Q factor
Before electroplating	21.3	128	2.06
Gold thickness: 9.5 µm	2.9	126	8.2
Gold thickness: 14 µm	1.7	125	16.6

Table 2.1: Electrical Characteristics of inductive stents (at the unexpanded state) with different gold coating conditions.

Device No.	Structural conditions	f_R in air (MHz)	Δf_R in saline (MHz)
1	with both thin gold (9.5 µm) and Parylene layer (8 µm)	49.7	-9.5
2	with thicker gold layer (14 µm) but thin Parylene layer (8 µm)	46.3	-8.2
3	with both thick gold (14 µm) and Parylene layer (30 µm)	47.1	-4.0

Table 2.2: Stent devices expanded in 6-mm-diemeter artificial artery prepared for their experiemntal evaluations.

It can be seen from the results that the effect of gold coating on resonance was significant given the dramatically enhanced amplitudes of the phase dips with the gold coated devices (#2 and #3). A comparison of the impedance spectra between air (Figure 2.3 (a)) and saline (Figure 2.3 (b)) cases indicates that their resonant behavior degraded when they were in saline (leading to reductions in the dip amplitude and broader bandwidth). By comparing between device #2 and device #3, the latter with a thicker insulation Parylene C layer was found to exhibit a substantially smaller shift of f_R (as shown in Table 2.2) as well as somewhat less saline impact on the amplitude of resonance dip in comparison with the case of the former device. The observed reductions in f_R were due to a high permittivity of the water-based medium, saline, which effectively increased the device's overall capacitance and thus reduced f_R. The degradation of resonance was presumably related to the damping effects caused by the electrical conductivity of the saline, in combination with capacitive shorting between the stent's inductive loops through the coating layer in the conductive liquid (which diminished as the coating thickness increased). A similar effect was reported in [36]. The observed outcomes illustrate that having a thicker insulation layer on the stent is important in reducing the influence of the conductive surrounding (saline, or blood in real application) on the resonant ability of the device (Similar to the gold layer, there is a limitation in the insulator thickness, as too thick layer will prevent stent expansion within a safe balloon pressure level – the largest thickness (of 30 µm) used in this study did not pose this type of expansion related issues.).

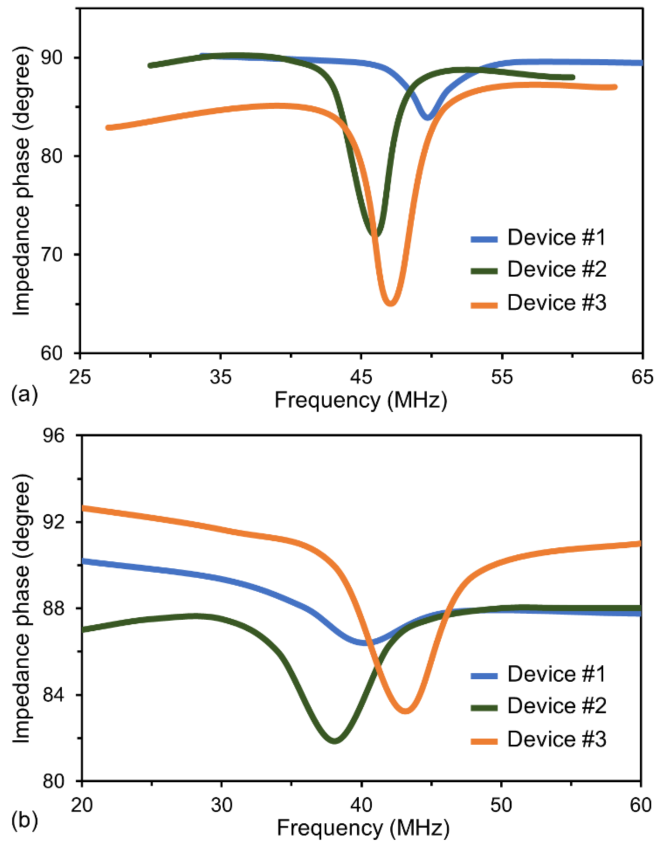

Figure 2.3: Phase dip measurements of here different stent devices #1-3 showing their resonant strength and frequencies (a) in air and (b) in saline.

2.3.2 Preliminary heating tests with wired power transfer

For the preliminary analysis of the effects of different coatings on the heating performance of stents, and to compare with the thermal behavior from wireless heating, device #1 to #3 were powered in a wired manner by coupling the device with the RF power amplifier directly. Each device was powered for its resonant heating in air with RF voltages (at f_R of each device). Moreover, wired heating was also performed with DC voltages for comparison purpose (except for device #2, as its only difference from device #3 was the presence of insulation layer that does not affect heating characteristics with DC/AC powering in air). An infrared (IR) thermal camera

(VarioCam HiRes 1.2 M, Jenoptik GmbH, Germany) was positioned above the stent device in the artificial artery to monitor and record its temperature map in real time. The RF and DC power values were determined by the voltage and current values measured from the stent device. The device temperatures measured with wired RF and DC powering are showin in Figure 2.4. In terms of RF powering, it can be seen from Figure 2.4 there is a clear difference between device #1 with the 9.5-µm-thick gold layer and the rest (devices #2 and #3) with the 14-µm-thick gold layer that exhibited significantly (>3 ×) higher heating efficiency than the former one. Devices #2 and #3 behaved similar, with slightly higher temeratures for the latter with a larger Parylene thickness. The DC powering results with devices #1 and #3 consistently proved that DC heating was less efficient than RF heating of those with thicker gold layers. These results indicate that gold coating was a critical parameter for enabling efficient heating that is uniquely available with the RF resonant scehme.

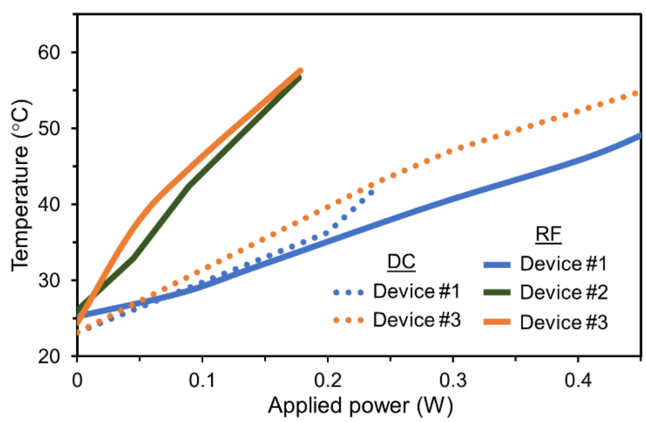

Figure 2.4: Wired testing results showing the maximum temperatures on the device-deployed artificial artery measured as a function of RF and DC powers applied to the device (RF powering was conducted at the f_Rs of the devices).

Given the results, device #3 was proven to be the most heating-efficient prototype and selected for further characterizations of RF heating performance, which was investigated with varying operation field frequencies around the particular f_R (47.1 MHz) of device #3, in three different surroundings as mentioned above to investigate their impacts on the heating performance for comparative analysis. For saline settings, the device-deployed artificial artery tube was connected with a pumped circulator (Polystat Standard 6.5 L Heated Bath, Cole-Parmer Canada, QC, Canada) with a saline bath at room temperature or body temperature to circulate the saline liquid to the stent device in the tube. The flow rate of saline was set to be 150 mL/min, which represents a blood flow rate of coronary artery under severe stenosis conditions [42].

Figure 2.5 displays the results obtained from this wired experiment, showing the stent temperature dependence on the applied power (Figure 2.5 (a-c)) and the operation field frequency (Figure 2.5 (d)) for each of the three surroundings. For the latter, the power was varied in each surrounding to limit or raise the maximum temperature (in air at 0.15 W or saline flow at 2.0 W, respectively) generated on the stent. The IR images of the heating stent (in the artificial artery) with these surroundings are shown in Figure 2.5 (e-g). As can be seen from Figure 2.5 (a-d), all cases exhibited the frequency-dependent heating which peaked at the measured f_R of the device in each surrounding (47.1 MHz in air and 43.1 MHz in saline – Table 2.2). The average rates of ΔT per applied power at resonance were 181 °C/W in air, 72.6 °C/W in static saline, and 3.3 °C/W in saline flow. The temperature amplitude in Figure 2.5 (d) decreased when the device surroundings are saline, especially saline flow. For example, the frequency selectivity of heating dropped in saline (this outcome can also be seen from the plots with varying frequencies in Figure 2.5 (a-c), in which, although the result at f_R of the device showed the highest heating in all surroundings, its superiority from the others at different frequencies decreased in saline). This phenomenon is presumably associated with the energy loss resulting from the capacitive coupling (via the Parylene C layer) between inductive loops of the stent, which became significant when the space was filled with saline, a conductive medium. This thermal result is consistent with the results observed in the electrical resonance measurement (Section 2.3.1). Another noteworthy feature (from, e.g., Figure 2.5 (d)) in saline ambience is that the power required to reach a certain temperature substantially increased with the presence of flow, which is the result of massive heat removal from the device due to the flow of saline liquid.

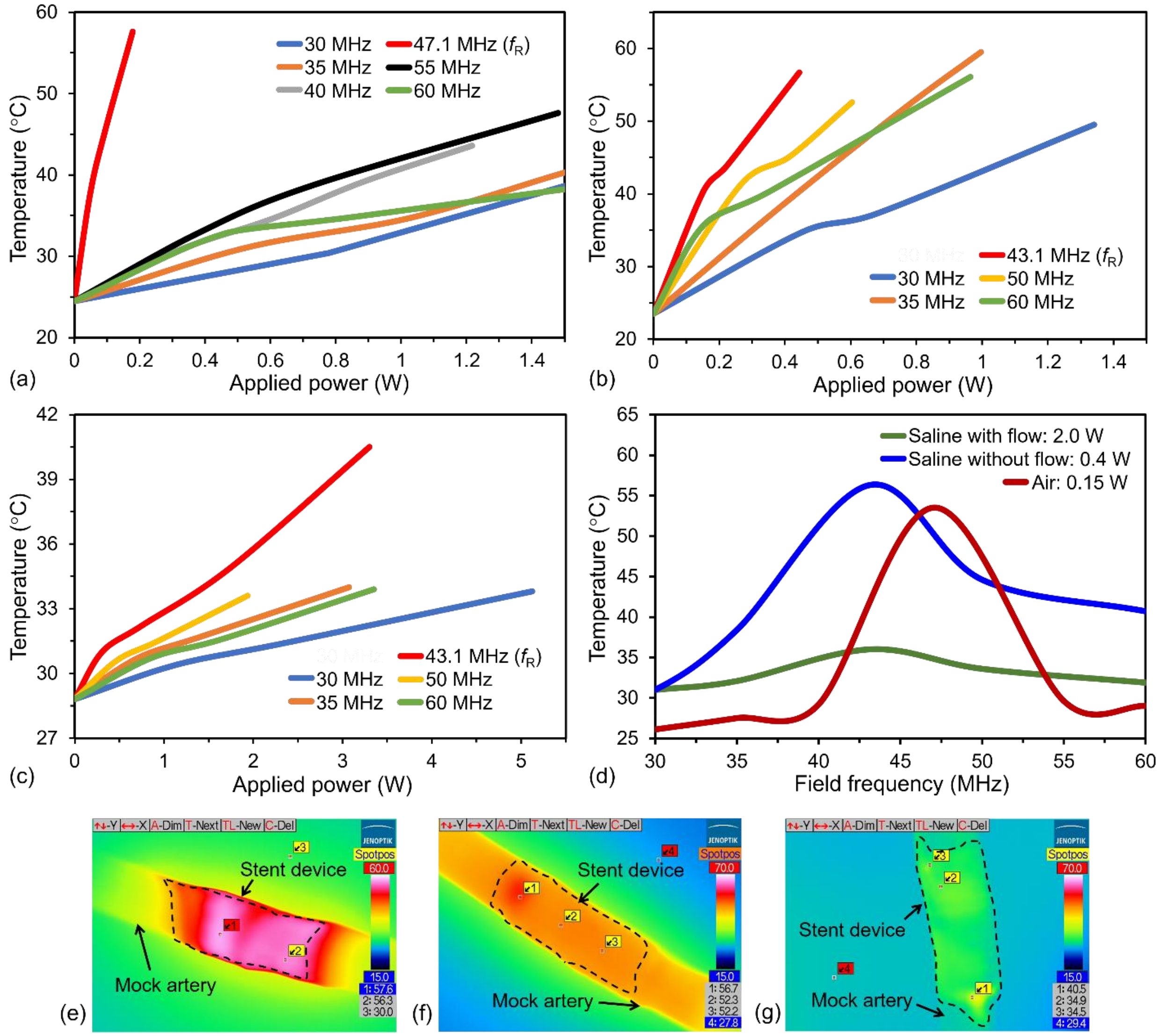

Figure 2.5: RF wired testing of device #3: (a)-(c) the maximum temperatures on the device-deployed artificial artery tube measured as a function of applied power at different frequencies including f_R in air, static saline, and saline flow, respectively; (d) frequency dependence of the tube's maximum temperature measured under the three different surroundings with adjusted power levels; (e)-(g) IR images of the artery tube under operation in air, static saline, and saline flow (with peak RF powers of 0.18 W, 0.44 W, and 3.3 W), respectively.

2.3.3 Wireless resonant heating in air and saline without and with flow

For the wireless heating of the device #3, the loop antenna discussed above was coupled to the RF power amplifier to produce the electromagnetic field, in which the stent device was excited and heated up wirelessly. As the power transfer level and resultant thermal output can vary depending on the orientation of the stent device with respect to the excitation antenna, to evaluate this aspect, the device was excited in following two different settings for comparative analysis: 1) the stent-deployed arterial tube was vertically positioned within the central region of the antenna loop, and 2) the stent/tube is positioned in parallel with the antenna loop around its center in close proximity. It should be noted that the parallel orientation involves higher clinical relevance as the arteries where stents are implanted tend to reside in parallel (rather than vertically) with the skin surface on which the excitation transmitter antenna is placed. These wireless experiments were conducted in the same three surroundings as used in the wired tests.

The measurement results with the vertical orientation from the same RF heating characterizations performed for the wired tests are presented in Figure 2.6. The results show all the characteristics observed in the wired test results, i.e., the frequency selectivity of heating and its frequency match with the measured f_R in each surrounding, as well as the damping effect in saline and its enhancement with the presence of flow. The results in Figure 2.6 (a-c) indicate the average ΔT rates per power of 167 °C/W in air, 62.6 °C/W in static saline, and 3.5 °C/W in the same saline flow at resonance. It can be seen from the figures that these rates at resonance are significantly higher than off-the-resonance rates, e.g., approximately up to 200× and 40× higher for air and saline flow ambience, respectively, than these cases when the field frequency was 7-8 MHz off from the resonance.

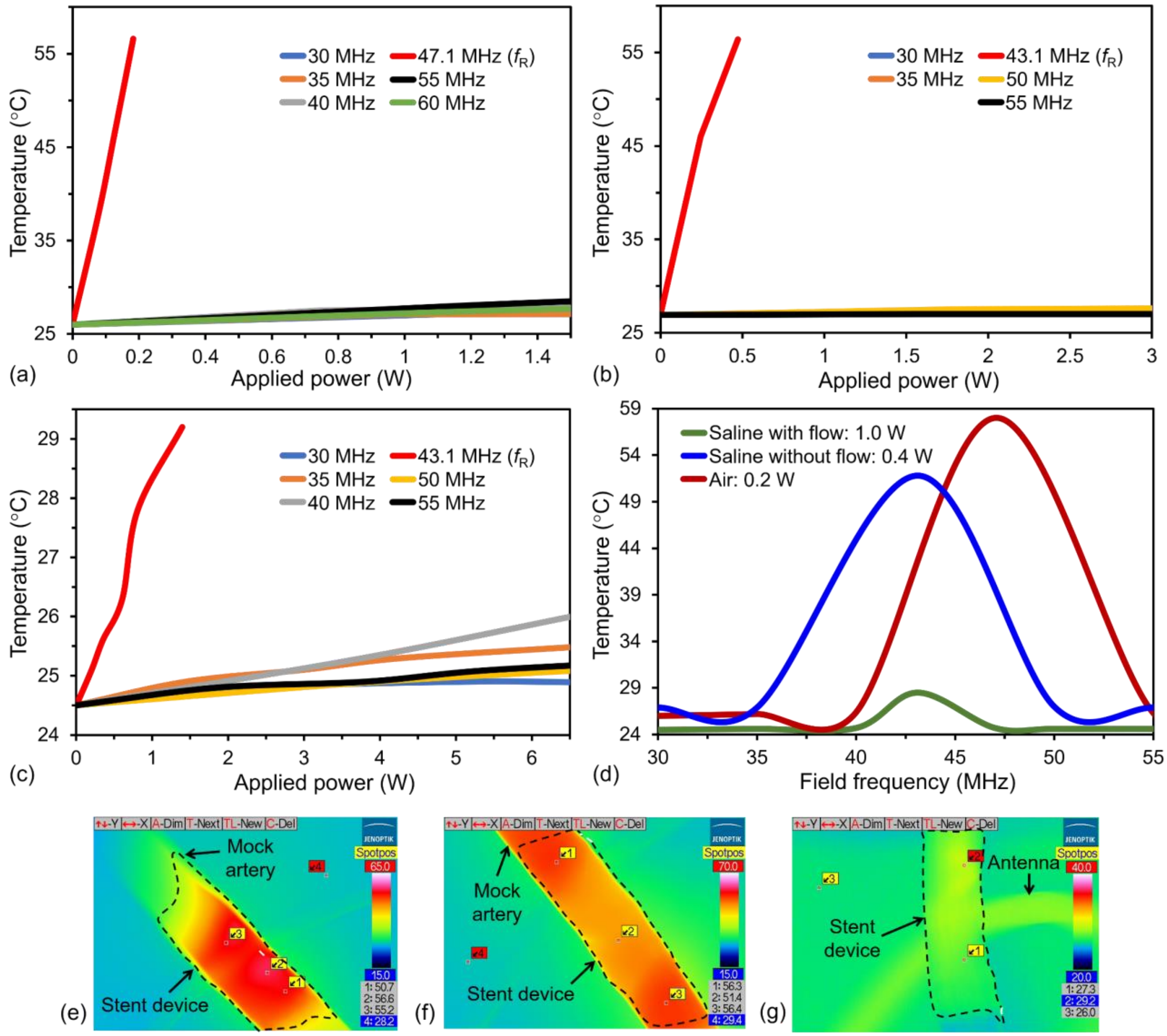

Figure 2.6: RF wireless testing of device #3 oriented perpendicularly with respect to the external antenna: (a)-(c) the maximum temperatures on the device-deployed artificial artery tube measured as a function of applied power at different frequencies including f_R in air, static saline, and saline flow, respectively; (d) frequency dependence of the tube's maximum temperature measured under the three different surroundings with adjusted power levels; (e)-(g) IR images of the artery tube

under operation in air, static saline, and saline flow (with RF powers of 0.18 W, 0.47 W, and 1.40 W), respectively.

In the case of wireless heating with the parallel orientation (Figure 2.7), the achieved temperatures tended to be lower than those obtained with the vertical orientation for given power inputs, with the average ΔT rates per Watt at resonance being 135 °C/W in air, 17.1 °C/W in static saline, and 1.1 °C/W in the same saline flow. The gains of these rates at resonance in air and saline flow (221 × and 43 ×, respectively) compared to the cases of off-the-resonance (by 7-8 MHz) were similar to those observed under the vertical orientation, which also means that the power had to be raised to compensate for the temperature reduction for the parallel orientation case. For example, with the saline flow, ΔT of + 2 °C needed a RF power of 1.6 W with the parallel orientation (Figure 2.7(d)), whereas it was reached with only 38 % of the power with the vertical orientation (Figure 2.6(d)). This outcome is reasonable considering the difference in electromagnetic interactions of the stent with the applied field between the two orientation scenarios. With the vertical orientation, there is a good match of the main field vector with the inductive axis of the stent, which results in an efficient EMF generation across the stent and resultant heating. However, this is not the case for the parallel orientation, in which the main field vector and the stent's inductive axis are orthogonal. Thereby, the EMF/heat generation has to rely on the fringing fields of which vectors match the stent's axis. Nevertheless, the measurement results indicate that the device with the parallel orientation exhibited consistent trends in terms of the field frequency and ambience as observed with the vertical orientation.

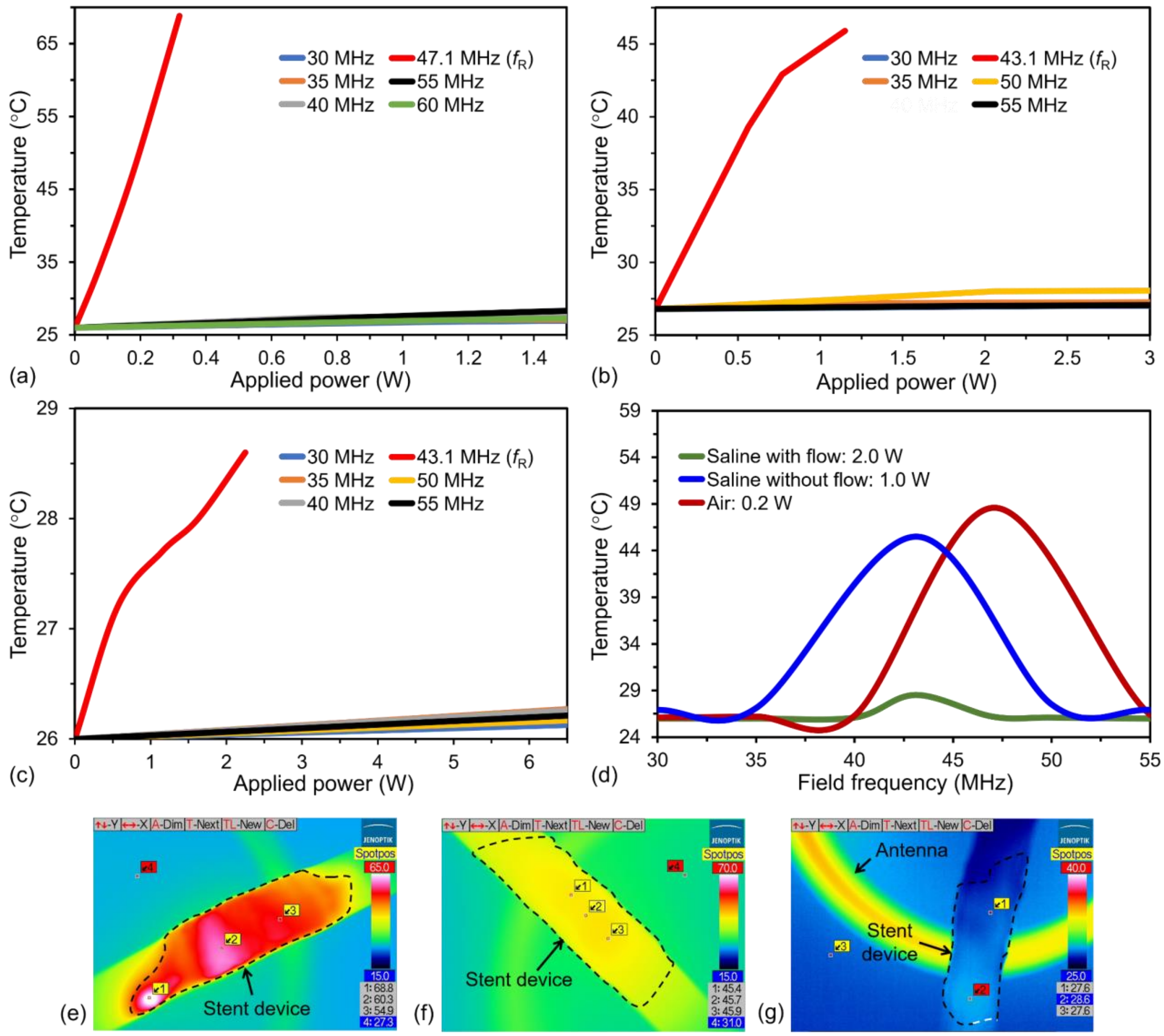

Figure 2.7: RF wireless testing of device #3 oriented in parallel with respect to the external antenna: (a)-(c) the maximum temperatures on the device-deployed artificial artery tube measured as a function of applied power at different frequencies including f_R in air, static saline, and saline flow, respectively; (d) frequency dependence of the tube's maximum temperature measured under the three different surroundings with adjusted power levels; (e)-(g) IR images of the artery tube under operation in air, static saline, and saline flow (with RF powers of 0.32 W, 1.15 W, and 2.25 W), respectively.

The heating efficiency of RF wireless heating at both orientations with respect to the wired case were calculated and analyzed using the obtained results with each surrounding. The particular efficiency here is defined to be the ratio of the wired power required to reach a certain ΔT to the wireless power required to reach the same ΔT in a selected surrounding. These powers were measured for reaching a ΔT of + 20 °C in air and static saline and + 3 °C in saline flow (Table 2.3). The calculated efficiencies for vertical and parallel orientations are plotted in Figure 2.8. As can be seen, the efficiency levels with the vertical orientation were in a range of 75 - 80 % for all three surroundings. In case of parallel orientation, the efficiency was 53 % in air and this dropped to 17 - 20 % in static saline and saline flow. The overall trend of higher efficiencies with vertical orientation is consistent with the measurement results as discussed earlier. The observed lower efficiencies in saline than that in air for parallel orientation suggests that the electromagnetic interaction with the stent device became lower with the presence of saline under parallel orientation. While the exact reason of this outcome is not clear, it might be related to the particular situation under this orientation that use fringing fields, which could have been substantially damped by the presence of saline to limit the excitation of the device. This hypothesis will require further in-depth analysis to verify.

Surrounding, ΔT	Wired power (W)	Wireless power - Vertical (W)	Wireless power - Parallel (W)
Air, + 20 °C	0.09	0.12	0.17
Static saline, + 20 °C	0.22	0.28	1.30
Saline flow, + 3 °C	0.58	0.76	2.95

Table 2.3: Summary of RF power levels required for three surroundings with defined ΔTs under different test settings.

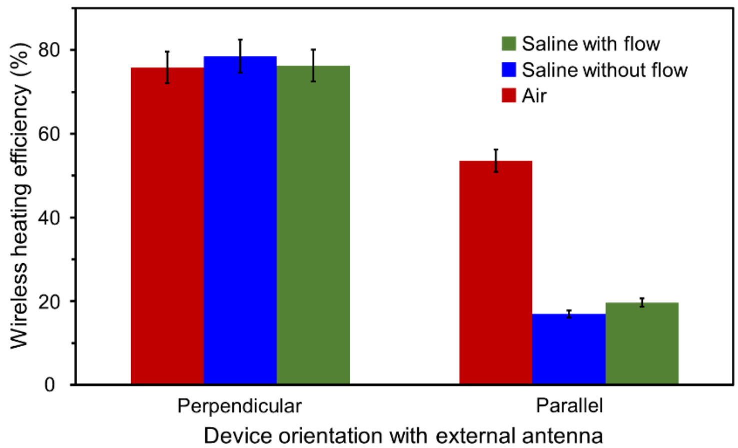

Figure 2.8: Wireless heating efficiency for perpendicular and parallel orientations under three different surroundings estimated using the results measured in the wired and wireless settings.

2.3.4 Wireless resonant heating with saline flow at body temperature

All previous tests with saline ambience were conducted at room temperature, while in real application, ambient temperature for the device is body temperature. In light of this, the following tests were performed using the same device (#3) by raising the saline temperature to 36 - 37 °C (in the bath of the circulator). In theory, ΔT for a given power should be independent on the ambient temperature as suggested in Equation (2). The thermal responses of the device with varying power inputs at resonance were measured for both orientations (The f_R level of the device showed no particular change due to the elevated saline temperature). The results shown in Figure 2.9 (a) indicate that the average ΔT rates per power for vertical and parallel orientations were 3.55 °C/W and 0.84 °C/W, respectively, both of which match well with those measured under room temperature (3.50 °C/W and 1.1 °C/W, respectively). This verifies the consistency of the device's thermal response with the theory with regard to ambient temperature. This is a beneficial feature in real application, in which the thermal output of the device will not be affected by possible variation of the background (body) temperature that can vary depending on individuals and particular conditions of the patients.

Using the same set-up at the elevated ambient temperature, heating performance was further tested to evaluate the temporal response of heating and its dependence on the flow rate of saline. As can be seen from the measured result in Figure 2.9 (b), the device showed fast heating rates by reaching their saturated temperature levels in 5-6 s upon powering, which were almost identical for both orientations. The blood flow rate in coronary artery in noncritical stenosis conditions was reported to range up to ~400 mL/min. To cover this possible flow rate range in different types of stenosis, three different saline flow rates (150, 300, and 600 mL/min) were tested (Figure 2.9 (c)), showing that ΔT consistently dropped with flow rate for both the orientations, as predicted. It is also worth noting that the difference between the ΔT values at the two orientations was nearly identical up to the flow rate of 300 mL/min and that this difference diminished as the rate further increased (to 600 mL/min).

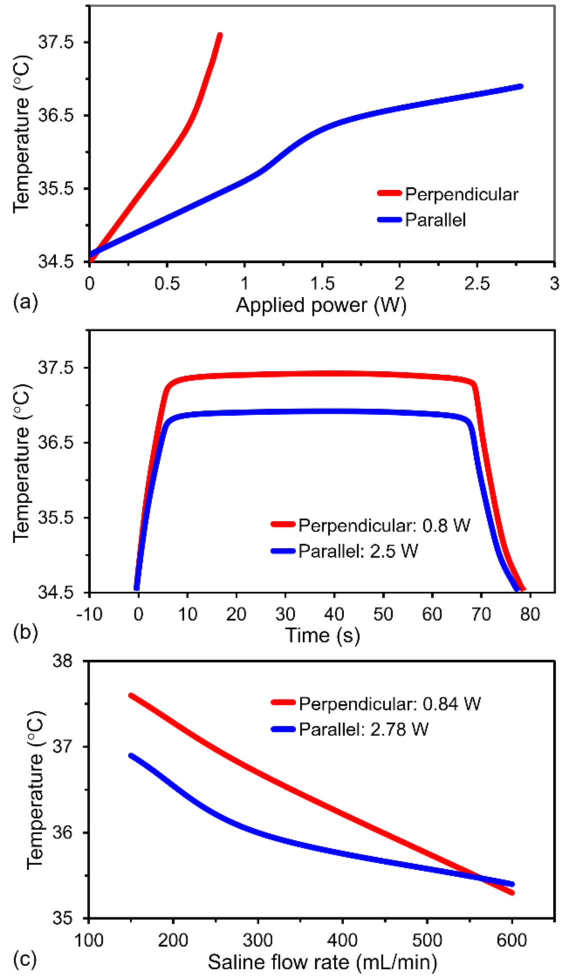

Figure 2.9: RF wireless testing of device #3 excited at resonance with both orientations under a flow of saline at near body temperature: (a) the maximum temperatures on the device-deployed artificial artery tube measured as a function of applied power with a flow rate of 150 mL/min; (b) temporal thermal responses of the excited device with adjusted powers levels; (c) the maximum temperature vs. saline flow rate with adjusted power levels.

Chapter 3: A MEMS Circuit Breaker for the Thermal Regulation in the Hyperthermia Treatment

3.1 Working principles and device design

As discussed in Chapter 2, this work also presents a thermo-responsive circuit breaker chip which is designed, microfabricated and integrated with the stent to work as a power switch that can manage the wireless heating of the stent device for the purpose of temperature control in the hyperthermia treatment. The circuit breaker developed in this study includes a Nitinol micro cantilever switch that can open or close the LC circuit of the stent device according to the surrounding temperature. When the temperature of the stent is above the safety threshold (50 °C), the Nitinol based cantilever actuator can immediately act to terminate the wireless heating by cutting off the LC circuit (Figure 3.1). The circuit breaker chip is also designed to incorporate a built-in capacitor, removing the need of integrating separately with the stent a thin film capacitor chip in Chapter 2.

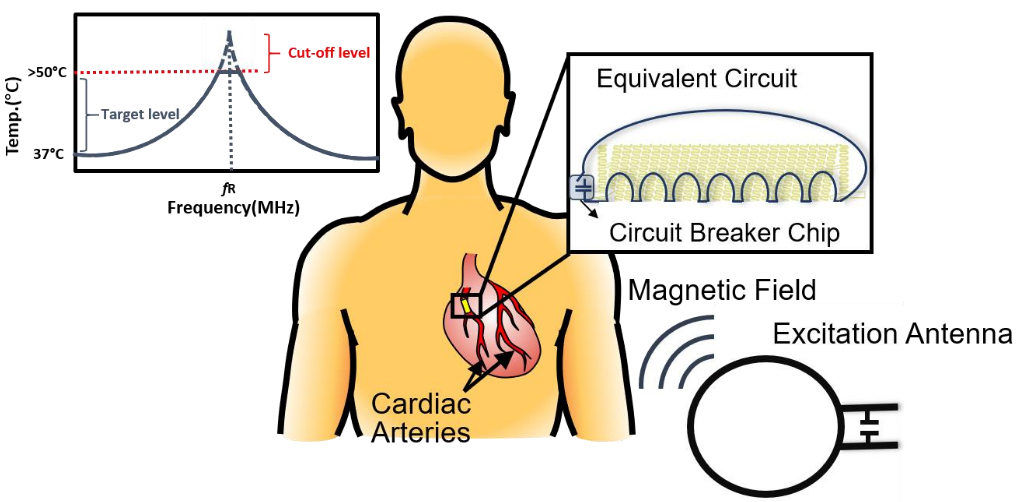

Figure 3.1: The stent device with circuit breaker for heat regulation in the wireless hyperthermia treatment for restenosis

The circuit breaker chip is a sandwich structure with the micro cantilever switch being located in the middle of the chip, the parallel-plate capacitor at the bottom and the lid on the top to seal the whole chip. Fabricated using Nitinol SMA, the micro cantilever switch can change its shape to open or close the circuit according to the surrounding temperature. Apart from the temperature shape memory effect, Nitinol has been demonstrated to have good biocompatibility, due to the formation of a passive Titanium-oxide layer (TiO_2) [43]. Nitinol SMA changes from austenite to martensitic phase upon cooling past its transition temperature. The temperature at which this martensitic transformation begins and completes are known as M_s and M_f, respectively. Accordingly, during heating, A_s and A_f are the temperatures at which the transformation from martensitic to austenite starts and finishes, respectively [44]. After being integrated with stent, the circuit breaker chip can sense the temperature from the heating of stent. In this study, a 220 µm-thick Nitinol sheet (Alloy M, Memry, Germany; austenitic start temperature (A_s) = 56.5 °C, austenitic peak temperature (A_p) = 68.5 °C, martensitic start temperature (M_s) = 53.5 °C) was used for the microfabrication of the cantilever switch part of the circuit breaker. As shown in Figure 3.2 (a) which is a detailed view of the cantilever (without showing the surrounding Nitinol frame), the circuit breaker is designed to incorporate a cantilever beam (800 × 100 × 10 μm^3) with a bossed tip (300 × 100 × 80 μm^3) at its terminal supported by the surrounding base frame (1900 × 700 × 220 μm^3). The bossed tip is designed to reduce the cantilever's actuation distance (and in turn switching time). A thin SiO_2 reset layer is designed to be deposited on top of the whole micro cantilever structure at high temperature. Due to their different coefficients of thermal expansion, after cooling off, the SiO_2 layer will induce a compressive stress to the cantilever beam, causing the cantilever beam to bend downwards. The SiO_2 layer was designed to be 4 μm thick according to previous work results [27, 28] so that the cantilever beam could bend down and come out of the base frame surface to be in contact with the bottom capacitor, forming a closed switch state. The mechanical behavior of the cantilever can be found in a similar model in [27]. A thin layer of gold (or copper) is also deposited on both sides of the cantilever structure (Figure 3.2 (b)) in order to make the top surface of the cantilever structure with SiO_2 conductive as well as to reduce the total chip resistance. The cantilever tip maintains its deformed shape in the Nitinol martensitic state, forming a closed switch at low temperature until the temperature rises above the threshold temperature A_s when the Nitinol begins to transition to the austenitic state. The cantilever will then stretch to its memorized flat shape. Therefore, the circuit breaker will be in an open state and cut off the LC circuit to prevent the power from being wirelessly transferred further to the stent device and the stent starts to cool off. When the temperature decreases again to M_s, the Nitinol cantilever will start returning to its martensitic state and bending downwards to touch the bottom capacitor and the circuit breaker will close the circuit again. Then the stent device begins to be heated up until the temperature reaches A_s.

The parallel-plate capacitor at the bottom of the micro cantilever switch is fabricated using medical grade 316L stainless steel sheets deposited by gold as electrodes and SiO_2 of 2 μm thick in the middle as the dielectric, which would theoretically give the capacitance of around 22 pF (with the plate area being 1.33 mm^2). A gold deposited 316L stainless steel sheet is bonded to the top of the micro cantilever to seal the chip, as shown in Figure 3.2 (b). It is important to note that, cantilever with both gold and copper coatings mentioned above are fabricated and studied in this work, however, for the coating of the capacitor electrodes and the top lids which also serve as the chip's packaging, gold is selected rather than copper as copper is not a biocompatible material.

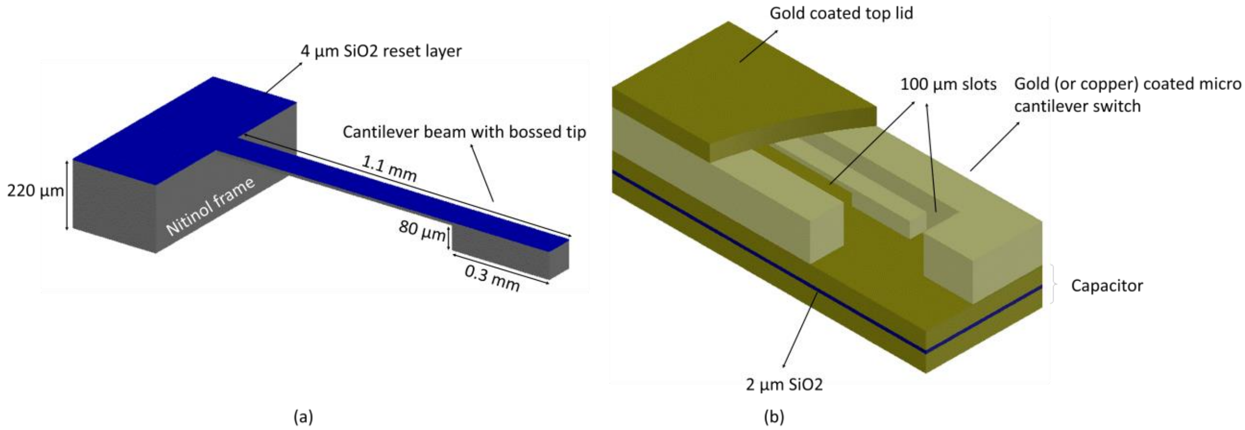

Figure 3.2: Design details of (a) the cantilever beam with a bossed tip, and (b) the complete circuit breaker chip.

For the characterization of the circuit breaker chip's thermal regulation performance, an inductive stainless-steel stent with gold coating in the unexpanded state is selected as the inductive component integrated with the circuit breaker chip. Therefore, after integrated with the unexpanded stent with inductance of 128 nH, the theoretical resonant frequency of the complete stent device with the circuit breaker chip is calculated to be 96 MHz. The gold layer thickness on the stent is supposed to be thicker than the skin depth at the operating resonant frequency of the resonant LC stent device for the purpose of minimized AC resistance and optimized Q factor of the stent device, as has been discussed in Chapter 2. As the theoretical resonant frequency of the stent device is configured to be 96 MHz, according to Equation 3, the skin depth of gold is calculated to be around 7.7 µm. In this study, an inductive stainless-steel stent is electroplated with

14 μm thick gold layer in the same manner as in Chapter 2. In addition, the top lid and the capacitor electrodes in the circuit breaker chip mentioned above are also electroplated with 14 μm thick gold layers for the same purpose.

As an outcome of the miniaturization of the circuit breaker chip with narrower cantilever beam and smaller electrical contact area between the cantilever tip and the bottom capacitor, the breaker switch will have a larger contact resistance during the actuation of the micro cantilever. Therefore, it is also important to reduce this negative effect for the stent device to become an effective resonator with the circuit breaker chip being integrated. Moreover, the circuit breaker chip with a larger contact resistance can cause a higher power consumption leading to a self-heating effect, which will be investigated and discussed in section 3.3.4. This is addressed by depositing gold (or copper) coating on the cantilever as noted above or using proper adhesive material (conductive epoxy) for the bonding of the capacitor with the micro cantilever switch, as will be discussed in section 3.3.2.

3.2 Fabrication

The fabrication process is shown in Figure 3.3, which starts from the micro cantilever switch part of the circuit breaker chip micromachined by the micro-electro-discharge-machining (μEDM; EM203, SmalTec International, IL, USA). First of all, the cantilever beam ($800 \times 100 \times 10$ μm^3) with the bossed tip ($300 \times 100 \times 80$ μm^3) is μEMDed by patterning a large cavity ($1100 \times 100 \times 140$ μm^3), followed by a smaller cavity ($800 \times 100 \times 70$ μm^3) within the previous larger cavity by using a 100 μm-in-diameter tungsten electrode. The last step of μEDM is the micromachining of three open slots of 100 μm wide using the same electrode along the surrounding of the patterned cantilever beam except the fixed end to release the cantilever beam from the Nitinol frame (Figure 3.3, step 1, (a)). Due to the repeated cycles of heating and cooling induced during the µEDM process [45], a residual tensile stressed layer is built within the surface of the patterned structure, resulting in a slightly curled cantilever beam after the µEDM step. Therefore, hydrofluoric (HF) acid is used to etch away the stressed thin layer on the Nitinol sheet and straighten the cantilever beam. Next, the Nitinol sheet with the patterned structure is ultrasonically cleaned for 90 minutes to remove all the surface residual particles or tiny substances formed in the µEDM and the HF etching processes that may affect the following SiO_2 deposition.

The SiO_2 deposition is performed by plasma-enhanced chemical vapor deposition (PECVD; TRION: PECVD & RIE, TRION Technology, AZ, USA) at 300 °C (Figure 3.3, step 1, (b)). The entire top surface of Nitinol sheet is next deposited with a SiO_2 layer for a thickness of 4 µm (Figure 3.3, step 1, (b)). After this deposition, the Nitinol sheet is kept at room temperature to cool off thoroughly, after which, due to the mismatch of the coefficient of thermal expansion, as noted above, the cantilever can be noticed bending downwards and coming out of the lower surface of the Nitinol sheet. Figure 3.4 (a) and (b) are the SiO_2 deposition results showing the top and bottom sides of the Nitinol sheet with the bending cantilever beam. To make the SiO_2 covered cantilever conductive (with a higher conductivity than Nitinol), 200 nm-thick gold (or copper) is deposited on both sides of the Nitinol sheet by electron-beam evaporation (Figure 3.3, step 1, (b)). For the gold evaporation, 20 nm-thick chromium was deposited as an adhesion layer prior to gold deposition to enhance the adhesion [46-48]. It is important to note that as the cantilever beam is only 10 µm thick, the gold (or copper) deposition should not be too thick in case of inducing extra stress to the cantilever, as it has been found in experimental trials that gold (or copper) layer thicker than 300 nm could cause a distortion of the cantilever structure. Figure 3.4 (c) shows the cantilever beam bending out of the surface on the Nitinol sheet with a gold coating thickness of 200 nm.

Lastly, the frame of the micro cantilever switch ($1900 \times 700 \times 220\ \mu m^3$) was cut off from the Nitinol sheet by using a laser cutting system (Compact Laser Micromachining System, Oxford Lasers, MA, USA). After the micro cantilever switch fabrication, the bottom surface of the switch is supposed to be completely insulated except the cantilever area, as the switch functions only by the cantilever displacement to open or close the circuit. For this purpose, Polyimide (PI) liquid (HD-4100, HD Microsystems, USA) is evenly applied onto the surface of the circuit breaker followed by the curing process done at 100 °C using the hot plate for 30 minutes (Figure 3.3, step 1, (b)).

In the capacitor microfabrication shown in Figure 3.3, step 2, firstly, a 316L stainless-steel sheet of 100 µm thick is electroplated with a 14 µm thick gold layer in the same manner as in [36]. Next, 2 µm thick SiO_2 is deposited on the gold coated stainless steel sheet by PECVD, followed by being laser cut to be 1900 µm long and 700 µm wide, which forms the capacitor electrode with the dielectric (Figure 3.3, step 2, (a)). Another same stainless-steel sheet electroplated with 14 µm thick gold is also laser cut to be the same size ($1900 \times 700 \times 100\ \mu m^3$). Next, two electrodes are bonded together with the SiO_2 in the middle by using conductive epoxy (CW 2400, Chemtronics, GA, USA) as the adhesive (Figure 3.3, step 2, (b)). Thereby, a parallel-plate capacitor with a theoretical capacitance of 22 pF (presuming the conductive epoxy layer serves as one of the electrodes) is formed.

Finally, the fabricated capacitor is coupled to the bottom of the micro cantilever switch using conductive epoxy or ethyl-cyanoacrylate (Figure 3.3, step 3, (a)). As a consequence, the capacitor serves as not only the capacitive component in the stent device but also the bottom lid to seal the whole circuit breaker chip. Bonding process involving the usage of conductive epoxy is done by heating the chip to around 100 °C for 20 - 30 minutes on a hot plate for accelerated cure and best epoxy conductivity, while the usage of ethyl-cyanoacrylate is totally a heat-free process. Figure 3.4 (d) is a microscopic image of the gold coated micro cantilever switch with its cantilever beam bending downwards and touching one of the electrodes of the capacitor integrated at the bottom. At last, another similar gold coated stainless steel sheet (1900 × 700 × 100 μm^3) used in the capacitor fabrication is bonded to the circuit breaker as the top lid using conductive epoxy as the adhesive (Figure 3.3, step 3, (b)). The overall size of the whole circuit breaker chip (as shown in Figure 3.5 (a), which shows the fully packaged chip placed on a Canadian 25 cents coin) including the micro cantilever switch, the capacitor and the top lid is measured to be 1900 × 700 × 605 μm^3.

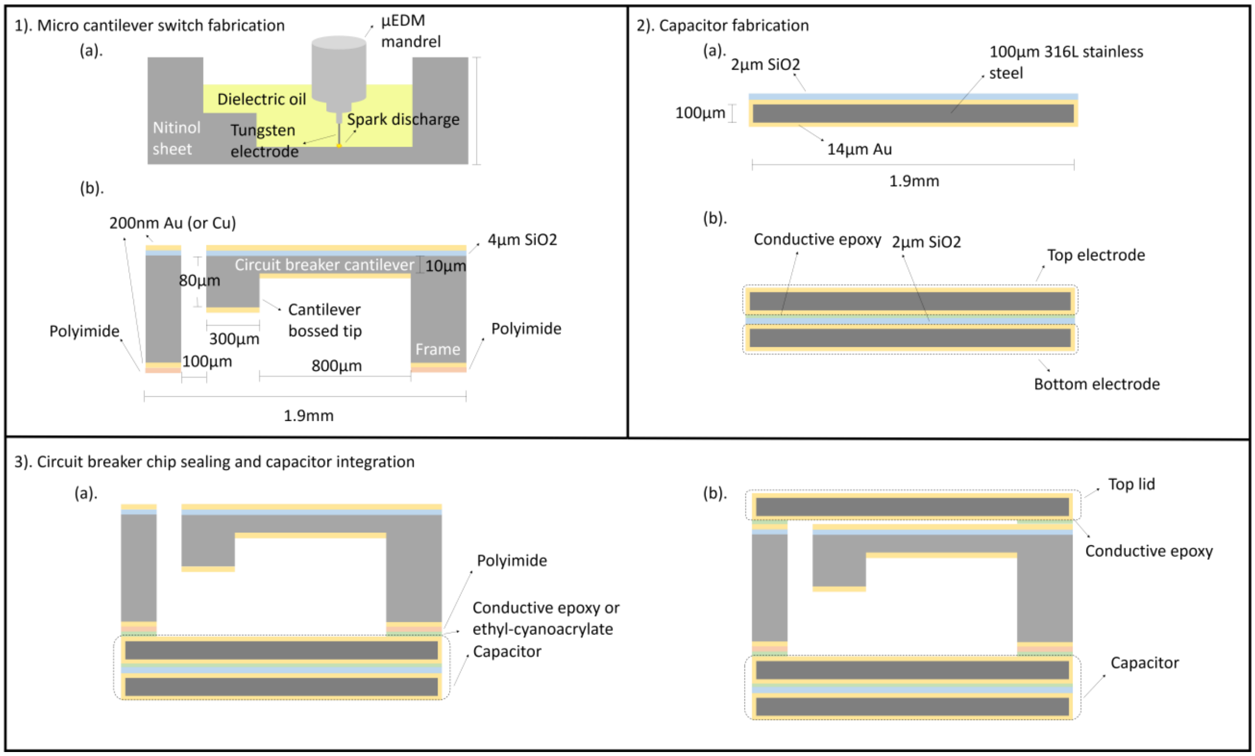

Figure 3.3: Microfabrication process of the circuit breaker chip.

Prior to the integration with the whole circuit breaker chip, the inductive stent is also gold electroplated in the same manner as discussed in Chapter 2 to deposit a 14 μm thick gold layer for operation in the expected resonant frequency (96 MHz) to guarantee a high Q factor inductor. Next, the circuit breaker chip bottom is mounted onto the one of the tab platforms of the gold coated stent (Figure 3.5 (b)) and interconnecting copper wire is bonded to the top of the chip and the tab platform on the other side of the stent using conductive epoxy cured at 100 °C for 20-30 minutes to form a series LC circuit, as shown in Figure 3.5 (c).

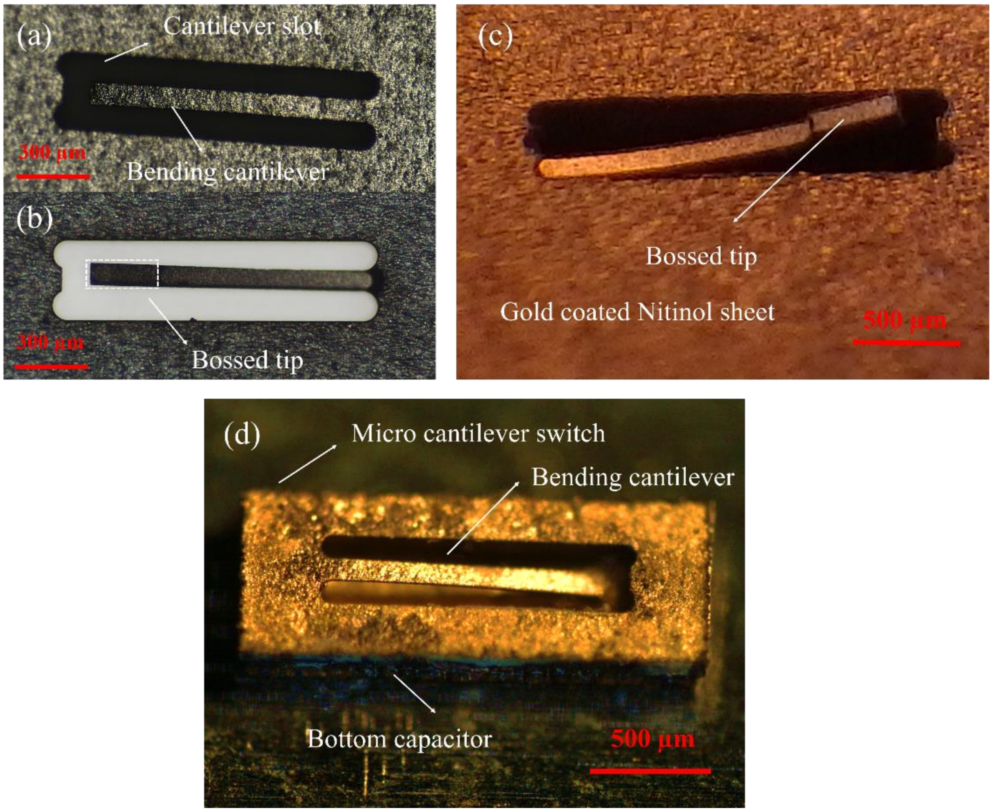

Figure 3.4: Microfabrication results: (a) the front side of the bended Nitinol cantilever deposited with SiO_2 on the top; (b) the back side of the bending cantilever; (c) the gold coated Nitinol cantilever bending out of the surface; (d) the gold coated micro cantilever switch with the cantilever touching the bottom capacitor electrode before the top lid integration.

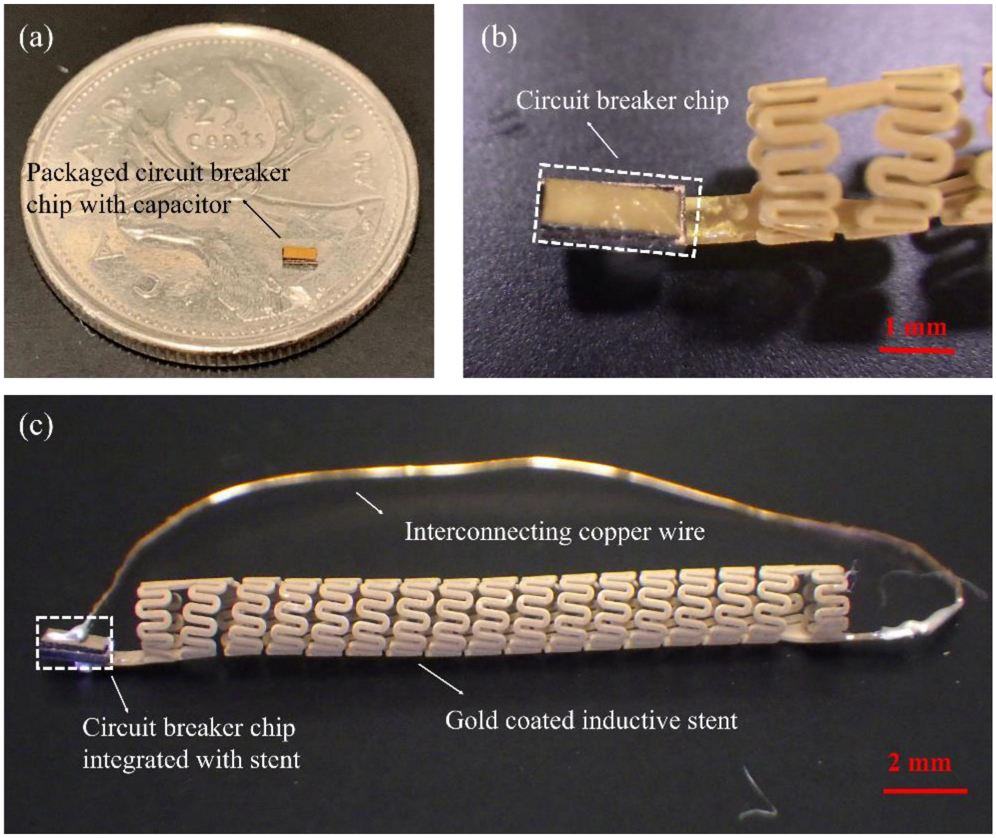

Figure 3.5: Stent device fabrication results: (a) the microfabricated and fully packaged circuit breaker chip placed on a Canadian 25 cents coin; (b) the circuit breaker chip bonded on the stent platform; (c) the complete LC stent device integrated with the circuit breaker chip.

3.3 Experimental results and discussion

The electrical and mechanical characteristics of the microfabricated circuit breaker, as well as the wireless heating experiments of stent device integrated with circuit breaker are presented and discussed in this section.

3.3.1 Thermomechanical behavior of circuit breaker cantilever

The thermomechanical performance of the cantilever beam was investigated by tracking the displacement of the cantilever beam during the heating and cooling process. As shown in Figure 3.6 (a), a laser displacement sensor system (LK-G32, Keyence Co., Japan) was used to track the cantilever tip position in a real-time manner, which was displayed directly on the reader of the sensor system and transmitted to an external computer. In the measurement, the Nitinol sheet was put on the hot plate upside down with the cantilever bending upwards and reaching out of the Nitinol frame surface. The hot plate temperature could be read from the display and a thermometer was also used to montior the temperature. The cantilever tip's initial vertical bending distance above the surrounding Nitinol frame surface due to the SiO_2 deposition was measured to be 75.1 µm. After, the sensor reading of the bending cantilever tip's initial position was zeroed and, by tracking its changing positions, the cantilever displacement at different temperature during the heating and cooling process were collected and plotted in Figure 3.6 (b). From Figure 3.6 (b), it can be observed that in the heating process when the hot plate heated up to around 60 °C which exceeded the Nitinol austenitic start temperature (As) 56.5 °C, the cantilever displacement started to increase more considerably than before until it stablized between 138.6 µm to 145.8 µm when the temperature reached 75 °C, a few degrees more than the austenitic peak temperature (Ap) 68.5 °C. When the heating source was removed, there was no monitored substantial decrease of the cantilever displacement until the temperature fell below around 60 °C, a few degrees above the martensitic start temperature (Ms) 53.5 °C. The shape recovery of the cantilever in the cooling process can be seen to be almost completed when the temperature dropped below 45°C. It can be concluded that all the cantilever transition temperatures measured in the heating and cooling experiment were close to the technically specified transition temperatures of the Nitinol sheet used for the circuit breaker fabrication.

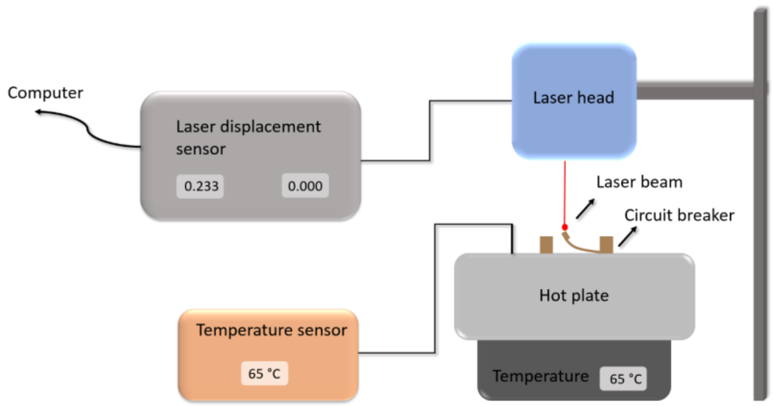

(a)

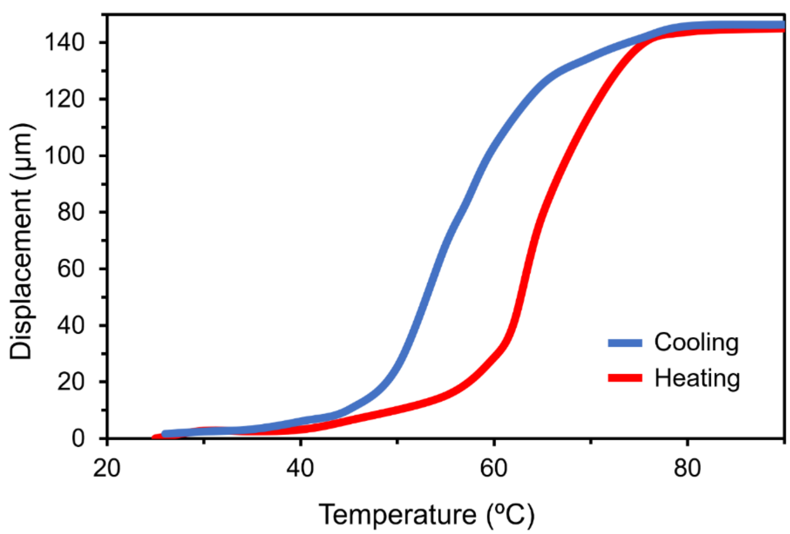

(b)

Figure 3.6: (a). The experimental set-up for measuring the displacement of circuit breaker cantilever at different temperature using laser displacement sensor; (b). The displacement of the cantilever during heating and cooling process.

Another important outcome observed from Figure 3.6 (b) is the cantilever tip position. Depending on the temperature, the cantilever tip can either be in contact or apart from the capacitor electrode (not yet integrated in this measurement set-up), which forms a closed or open switch. It can be seen that before heating, the cantilever tip would be in electrical contact with the capacitor electrode, forming a closed switch. When the temperature of the cantilever was raised about 65 °C, its tip was displaced, breaking contact with the capacitor electrode and forming an open switch. Upon cooling to below 57 °C, the electrical contact was reformed when the cantilever tip was reset to its original position, closing the switch again.

3.3.2 Electrical switching behavior of the circuit breaker

Figure 3.7 shows the eletrical responses of the circuit breakers characterized by measured eletrical contact resistance between the cantilever tip and the bottom electrode while the chip was being heated from room temperature to 80 °C and then cooling back to room temperature. One significant feature can be noticed is the temperature dependence of the contact resistance during the heating and cooling process. As can be seen from Figure 3.7, in the heating process, there was almost no substantial resistance increase among three circuit breakers (with different coating and adhesive materials – to be discussed later) until the temperature rose up to around 55 - 60 °C which is close to As of Nitinol (56.5 °C). A sharp contact resistance rise can be noticed until the temperature reached around 65 °C at which resistance increased beyond the measurable range, which indicated that the electrical contact between the cantilever and the bottom capacitor was lost and the circuit breaker was in an open switch condition. During the cooling process, it can be seen that the contact resistance was obtained again when the circuit breaker cooled off to around 60 °C and a sharp resistance decrease can be noticed until the temperature dropped to 50 °C at which the contact resistance remained as low as it was prior to heating and a fully closed switch was formed. It can be noticed that all the threshold temperatures at which the circuit breaker switched to different conditions (close/open) measured in the experiments match with those noted in thermomechanical behavior as discussed above, as well as the technically specified transition temperatures of the Nitinol sheet used for the circuit breaker. These electrothermal behavior, together with the thermomechanical characteristics discussed above, all demonstrated the intended functionality of the circuit breaker.

Another noteworthy feature that can be seen is the dependence of the contact resistance on the metal coatings and adhesives used for the chip fabrication. Although the thermomechanical characteristics of the cantilever described in section 3.3.1 are only dependent on the properties of the Nitinol cantilever and SiO_2 layer, the electrothermal behaviors are results of not only the Nitinol cantilever but the metal coatings as well as adhesive materials.. Metal coatings of the circuit breaker, with their different properties of electrical conductivity and thermal stablity over a large temperature range required in the chip fabricaiton process involving high temperature (100 °C) heating including PI curing and bonding using conductive epoxy, play an important role in the electrothermal behavior. For example, prior to heating the copper coated circuit breaker had initial contact resistance of 31.2 Ω (Figure 3.7 (b)) at room temperature (26.5 °C) while the resistance of gold coated circuit breakers were measured to be 3.4 Ω (Figure 3.7 (c)) and 3.3 Ω (Figure 3.7 (d)), respectively. It can be concluded that circuit breakers with gold coating had significantly lower contact resistance than that with copper coating, although both the copper and gold coatings were effective in limiting the chip resistance, compared to the case without any metal coating (leading to the initial breaker resistance of 70.5 Ω) (Figure 3.7 (a)). Given the fact that the conductivity of copper (5.98×10^7 S/m) and gold (4.52×10^7 S/m) are close, the significant difference of the circuit breaker chip resistance might be the result of copper oxidation forming during the PI curing process of long duration (30 minutes) at high temperatures (100 °C), respectively, as a previous study [49] found that at temperatures close to 100 °C, copper oxidation composition Cu_xO begins to form on copper surface. In comparison, although relatively more expensive in cost, gold deposition offers much lower contact resistance in high temperature and better protection against corrosion than copper (as backed by the fact that most of MEMS contact switches have used gold as the contact material [50, 51]), which contributes to lower chip resistance for long-term application in the artery hypertherima treatment. Apart from the metal coatings, the adhesive material used for capacitor (bottom electrode/lid) bonding also contributes to in the overal chip resistance. In this study, two different adhesives, i.e., conductive epoxy and ethyl-cyanoacrylate were studied and their effects on the contact resistance are shown in Figure 3.7 (c) and (d). Figure 3.7 (c) shows the measured resistance of the gold coated circuit breaker with ethyl-cyanoacrylate as adhesive during two rounds of heating and cooling process. The initial resistance of the circuit breaker chip was measured to be 3.4 Ω before heating but rose up to 5.3 Ω after cooling. The final resistance of the chip after being heated up and cooled off to room temperature again was measured to be 10.2 Ω. Additionally, it can also be seen that the resistance plots of the 2nd cycle of heating and cooling process were overally left-shifted, indicating that the contact resistance were also larger than before at elevated temperatures. In contrast, the circuit breaker chip with same gold coating but using conductive epoxy as adhesive has an initial resistance of 3.3 Ω prior to heating but only 3.5 Ω after cooling and 3.6 Ω after 2nd heating and cooling process. At elevated temperatures, the resistance plots of two different cycles of heaing and cooling process can be found to almost overlap with each other (Figure 3.7 (d)), indicating that the resistance remained relatively constant within a large range of temperature change. The reason behind that ethyl-cyanoacrylatewhy bonded circuit breaker exhibited larger contact resistance after heating might be the depolymerization of the cured ethyl-cyanoacrylate upon heating (above 80 °C) and re-deposotion (re-polymerization) of the vapor phase polymer onto the contact area of the cantilever tip and capacitor electrode during the thermal process [52-54].

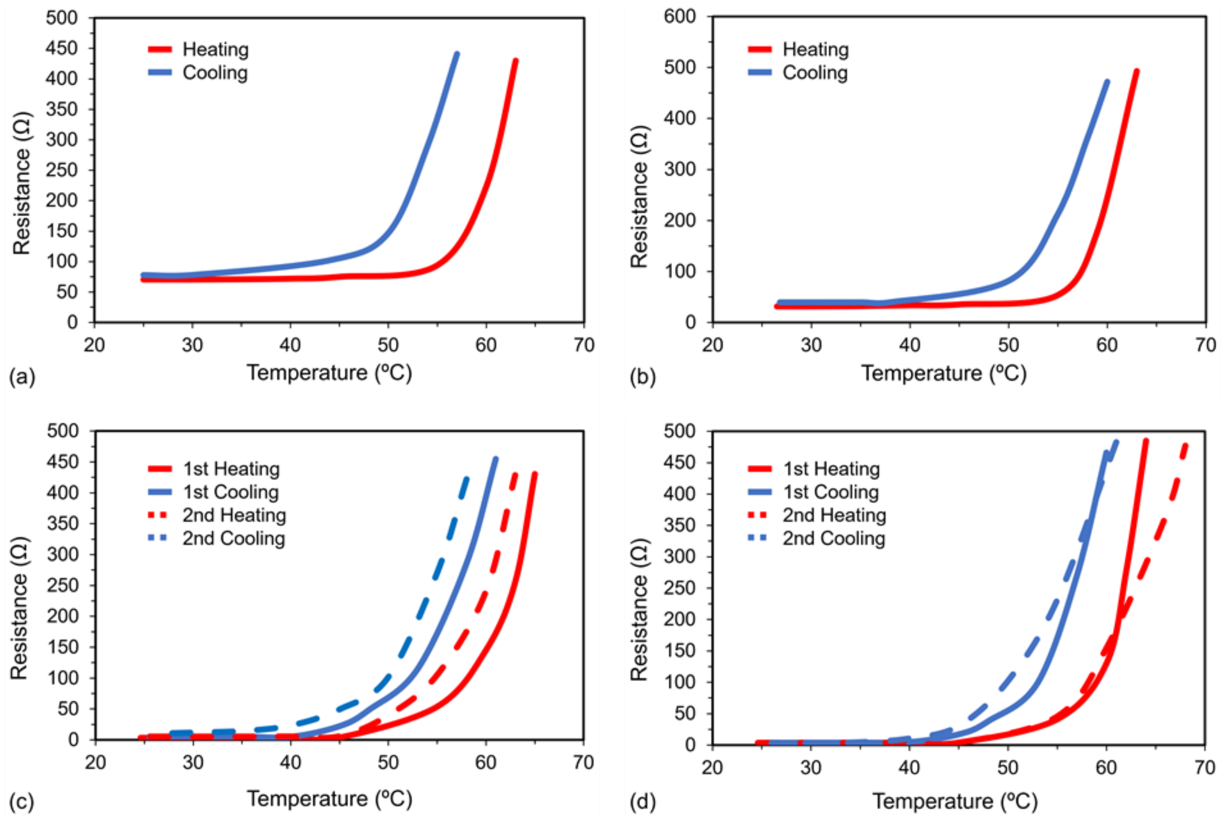

Figure 3.7: Contact resistance of circuit breakers from room temperature to 80 °C with (a) no metal coating and ethyl-cyanoacrylate as adhesive; (b) copper coating and ethyl-cyanoacrylate as adhesive; (c) gold coating and ethyl-cyanoacrylate as adhesive measured in two cycles of heating and cooling processes; (d) gold coating and conductive epoxy as adhesive measured in two cycles of heating and cooling processes.

3.3.3 Electrical characteristics of the stent device with the circuit breaker chip

The electrical characteristics of the integrated stent devices used for wireless heating tests are summarized in Table 3.1. As discussed above, all three stent devices had the same type of inductive stents with a gold layer of 14 μm, but coupled with circuit breakers that have different metal coatings and adhesives. As it can be seen from the table, the inductive stents with gold coating (without the circuit breaker chip integrated) have much lower resistance of only 1.6 - 1.7 Ω and higher Q factors of 16.9 - 17.2, compared to the original resistance 21.3 Ω and Q factor 2.06 of the stainless-steel stent. The resonant frequencies of three integrated stent devices were measured using the spectrum analyzer (4396B, Agilent Technologies, CA, USA) in a wireless manner by having an inductive coupling between the stent and a reader antenna connected to the spectrum analyzer, as shown in Figure 3.8. Three stent devices were measured to have a resonant frequency from 103.3 MHz to 107.7 MHz, with the theoretical resonant frequency being 96 MHz as mentioned above. The difference between actual and theoretical resonant frequency might be the result of the inaccuracy of SiO_2 deposition process and the existence of the parasitic capacitance within the stent device. It can also be observed from Figure 3.8 that the device #2 and device #3 with lower chip resistance exhibited stronger resonance characterized by enhanced amplitudes of phase dips than device #1 with larger chip resistance, which implies that the wireless power transfer would be more efficient for the devices #2 and #3 than device #1, according to the findings in Chapter 2, and also explains why limiting the chip resistance is critical for this application.

Device No.	Circuit breaker characteristics	Stent Resistance (Ω)	Stent peak Q factor	Circuit breaker resistance (Ω)	Resonant frequency (MHz)
#1	Cu coated with ethyl-cyanoacrylate	1.6	17.2	31.2	107.7
#2	Au coated with ethyl-cyanoacrylate	1.7	16.9	3.4	103.3
#3	Au coated with conductive epoxy	1.7	16.9	3.3	106.1

Table 3.1: Summary of LC stent devices (at unexpanded condition) studied in the wireless heating tests.

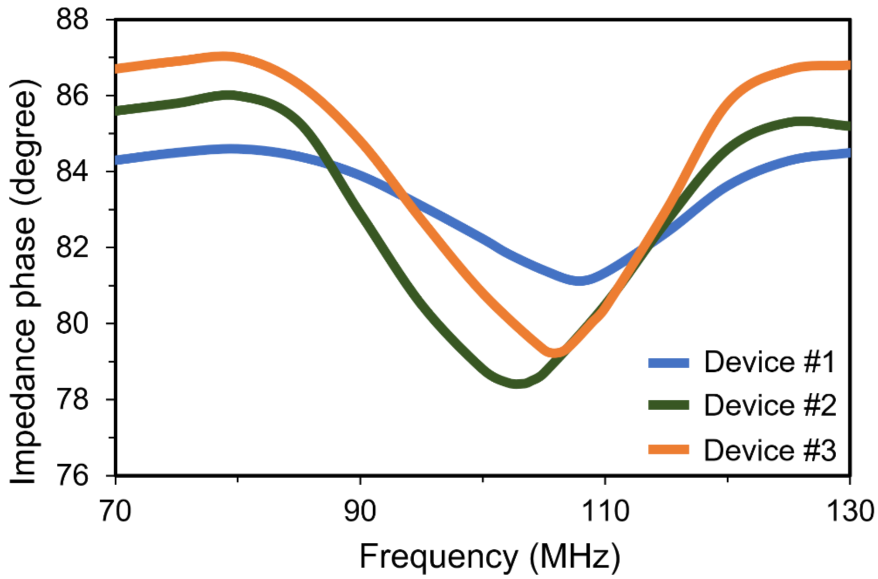

Figure 3.8: Resonant frequencies of three LC stent systems characterized by the measured impedance phase dips.

3.3.4 Wireless heating of the resonant stent device with circuit breaker for heat regulation

As the intended use of this proposed stent device with circuit breaker for heat regulation is safeguarded wireless hyperthermia treatment against stenoid coronary arteries, preliminary tests of wireless heating of circuit breaker integrated stent devices were performed to investiagte on the thermal behaviors of the stent and the funtionality of the circuit breaker as a power switch. A round-shaped loop antenna made of same thick copper wire (14 AWG) as used in Chapter 2 with inductance measured to be 88.5 nH with a diameter of 4cm was prepared as the power transmitter in the RF wireless heating system. A capacitor of 25 pF was coupled in parallel with the antenna to match its resonant frequency f_R (106.5 MHz) with the stent devices (103.3 - 107.7 MHz). The same experimental set-up described in Chapter 2 (Figure 3.9) was utilized to for the wireless heating tests of the stent device with circuit breaker. In the tests, the stent device was located in parallel with the power antenna (which would be closer to actual clinical settings as noted earlier) around its center at close proximity. The power consumption of the excitation antenna were also calculated using the voltage and current values measued by the oscilloscope.

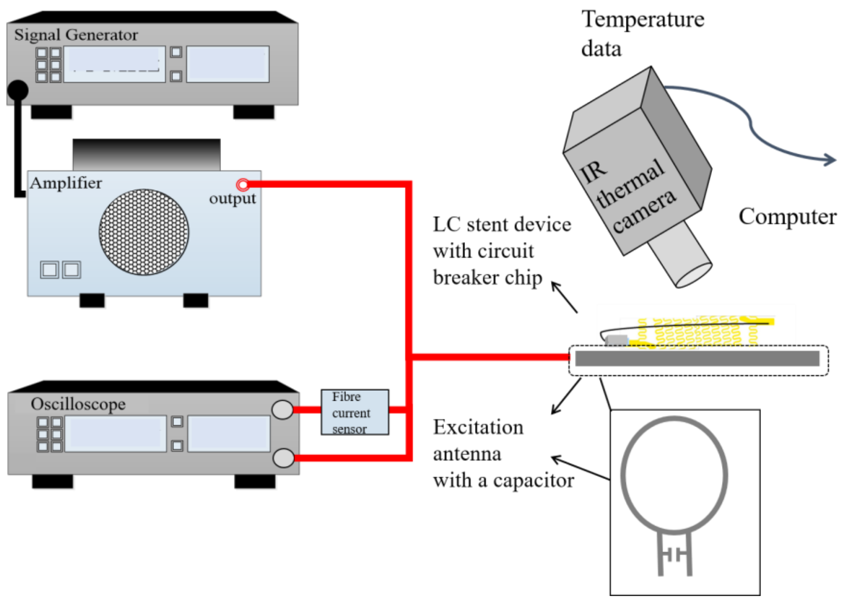

Figure 3.9: Experimental set-ups for the wireless heating experiments of the stent device integrated with the circuit breaker chip.

For the wireless heating tests, three stent devices (#1, #2 and #3) mentioned above were tested in air ambience and compared with respect to their thermal behaviors. To power the stent device, RF power of 1.2 W was provided to excitation antenna. Figure 3.10 displays the results of five heating-cooling cycles tested with three devices. The temperature change with time on the stent surface as well as the circuit breaker were recorded and the corresponding circuit breaker chip status (open/closed) was labelled in the figure. Prior to the tests, the initial room temperatures of three stent devices (#1, #2 and #3) were measured to be 28.8 °C, 27.4 °C and 26 °C, respectively. In terms of their functionality for heat regulation, it can be observed from Figure 3.10 that all circuit breakers of three devices exhibited similar thermo-responsive performance. For instance, in the initial closed state at the beginning, the temperature of three circuit breakers kept increasing from room temperature until it reached around 65 - 69 °C in less than 20 seconds. Afterwards the circuit breaker chips switched to open condition to terminate heating and the temperature of circuit breakers started to drop until around 52 - 57 °C in around 5 seconds. The repeated on-off cycles were observed to be consistent. From these observations it can be concluded that, as a power switch, all circuit breakers functioned as intended as the temperature at which the chips switched between open (65 - 69 °C) and closed (52 - 57 °C) status all matched with their transition temperature characterized in the thermomechanical and electrical behaviors as discussed above. Furthermore, the temperature change of each stent was also in synchronization with that of the circuit breaker chip, indicating that the circuit breaker could initiate and terminate the wireless power transferred to the stent by closing and opening the LC circuit. Despite the similarities with respect to the thermal regulation behavior of circuit breakers, it can be noted from Figure 3.10 that three stents exhibited different temperature levels during the heating and cooling. For the device #1, the peak temperature of the stent during the heating ranged from 33.8 °C to 34.1 °C, which was 5 - 5.3 °C increase from room temperature. In contrast, device #2 had a peak temperature around 35.9 – 37.1 °C with temperature increase of 8.5 - 9.7 °C, while for device #3, the peak temperature reached 42.2 - 44.6 °C and the temperature increase was 16.2 - 18.6 °C. Figure 3.11 (a) and (b) show the infrared images of device #3 (Figure 3.10 (c)) with the peak temperature (67.8 °C on the chip, 42.2 °C on the stent) and the lowest temperature (54.8 °C on the chip, 41.3 °C on the stent) during the 1st cycle (Figure 3.10 (c)). Despite that all circuit breakers showed similar thermal characteristics, the stent of device #3 demonstrated the highest temperature increase whereas the stent of device #1 showed the lowest temperature rise with the same RF power (1.2

W). It can be inferred from above that the higher resistance of copper coated circuit breaker in device #1 would result in its more power consumption and self-heating within the breaker chip (rather than in the stent), represented by higher temperature increase of the copper coated circuit breaker but lower of the integrated stent. Moreover, in spite of similar initial resistance of gold coated circuit breakers in device #2 and #3, device #3 demonstrated closer temperature increase of the stent, which verifies that the ethyl-cyanoacrylate used as the chip adhesive in device #2 induced larger resistance upon heating, as already shown and discussed in Section 3.3.2. From what has been observed and analyzed above, it can be concluded that (1) gold is a more appropriate material than copper for the circuit breaker's coating to reduce the resistance presumably due to the presence of copper oxidation composition forming in high temperature (70 °C), and (2) the use of conductive epoxy as adhesive for the bottom sealing of the circuit breaker chip could prevent additive resistance resulting from the use of ethyl-cyanoacrylate. In addition, this preliminary study has verified the feasibility of the miniaturized circuit breaker design prototyped in this study for automatic thermal regulation of wireless heating stent towards its hyperthermia application.

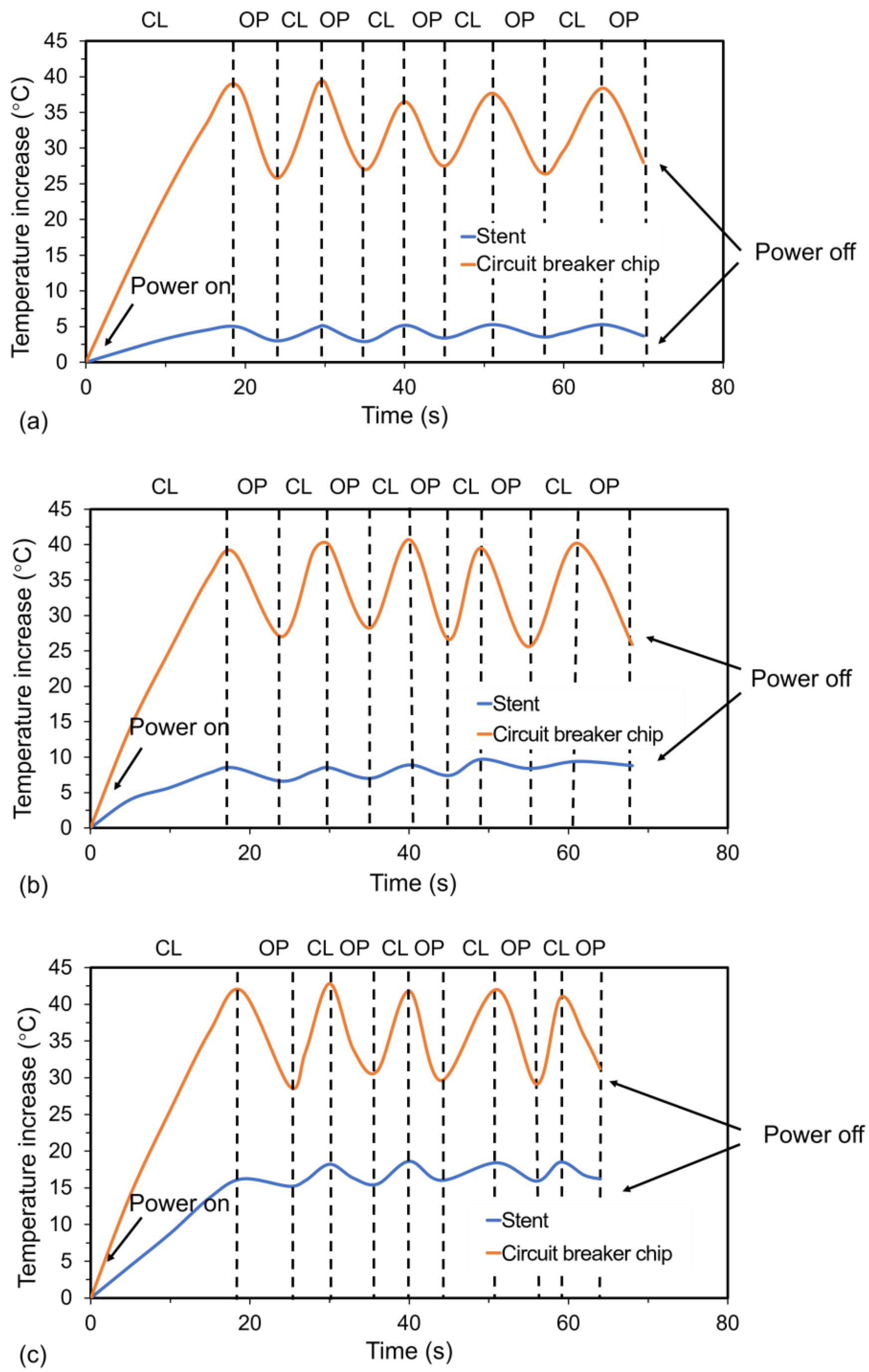

Circuit breaker status: CL= Closed; OP = Open

Figure 3.10: Wireless heating results showing self-regulated temperature control by circuit breaker in stent devices (a) #1, (b) #2, and (c) #3 with the power input of 1.2 W.

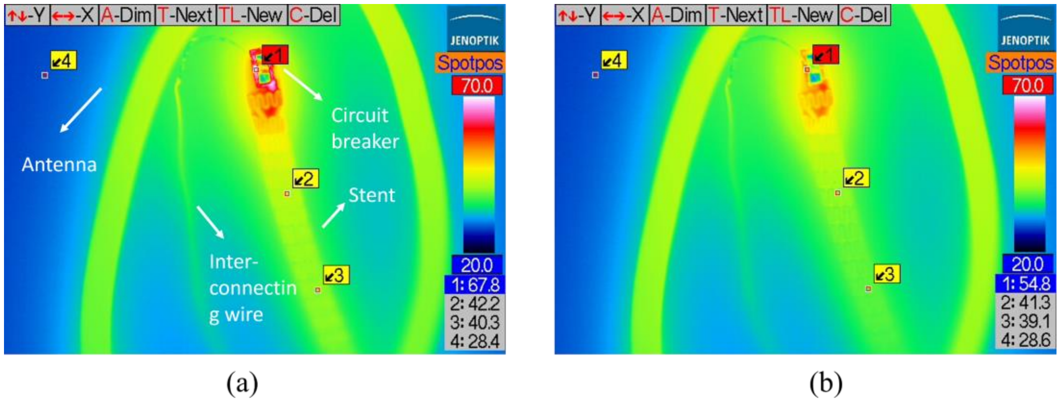

Figure 3.11: IR images of thermal characteristics of the device #3 wirelessly powered by external antenna with (a) the peak temperature; (b) the lowest temperature during the 1st cycle.

Chapter 4: Conclusions and Future Work

Firstly, this work has experimentally studied a LC-tank-based resonant stent device developed for wireless endohyperthermia treatment application. Optimized coating of gold and Parylene C on the inductive stent was shown to improve resonant behavior and thermal output of the device. Wireless powering of the stent device using tuned external RF fields was tested to investigate on the heating performance of the developed prototype in both air and saline under varying conditions of relevant parameters including RF power, field frequency, stent orientation, and saline flow rate. The wireless results clearly indicated the benefit of resonant powering and heat production, with heating rates increased up to two orders of magnitude from those obtained with several MHz off the resonance. Wireless heating efficiency was evaluated along with wired powering tests. The measurements with saline flow at near body temperature also showed that, as theoretically predicted, wireless heating performance was almost independent of ambient temperature. The temperature increases obtained in saline at a stenotic flow rate were approximately 2-3 °C with RF powers less than 3 W in both stent orientations, respectively. A preferred path to reaching the target temperature level for restenosis hyperthermia will be to raise the heating efficiency of the device in saline flow, rather than increasing RF power for the sake of suppressing electromagnetic radiation to a stented patient. Potential approaches to improving the wireless heating efficiency include: (1). enhancing the resonance of the stent device in saline ambience (e.g., thickening the Parylene C coating on the stent to reduce capacitive shorting effects while optimizing the thickness for effective mechanical expansion of the stent); (2). optimization and design on the power transmitter side (excitation antenna) for enhanced electromagnetic interaction with the stent device and therefore, higher heating efficiency. One possibility is to design a transmitter with multiple independent loop antennas in several directions to increase the magnetic flux that pass through the stent in parallel with its longitudinal inductive axis.

Secondly, a miniaturized chip (1900 × 700 × 605 μm^3) of thermo-responsive MEMS circuit breaker which consists of a micro cantilever switch and a capacitor has been designed, fabricated and studied experimentally with regards to its electrothermal, thermomechanical, as well as heat regulation performance in the wireless heating after being integrated with a gold coated inductive stent to form a LC resonant heater. The circuit breaker power switch was designed to incorporate a cantilever beam deposited with SiO_2 on the top side that makes the cantilever bend downwards. The micro cantilever beam structure was μEDMed using Nitinol to utilize its temperature-dependent shape recovery feature to function as a temperature-sensitive power switch that could automatically close or open the LC circuit for heat regulation purpose. The circuit breaker was gold (or copper) coated and other components including electrodes were all electroplated by gold with thickness above the gold skin depth at the working resonant frequency to limit the AC resistance and achieve higher wireless heating efficiency. Studies of the thermomechanical and electrothermal behavior of circuit breakers have verified the intended functionality of the circuit breaker. The wireless heating performance of the LC stent device with circuit breaker chip were also investigated and experiment results demonstrate that the miniaturized circuit breaker was capable of automatically regulate wireless heating of the stent device. Moreover, studies of different circuit breaker chips suggest that gold coated circuit breaker with conductive epoxy bonding assembly is a suitable approach to mitigating self-heating effect and in turn transferring more power to stent heating.

Future work will focus on how to further reduce the chip resistance for the purpose of enhanced heating efficiency as well as uniform temperature increase on the chip and stent. Possible paths to this goal include: (a). Optimization of gold deposition methods towards thicker gold layer for the sake of lower AC resistance while maintaining the intended thermomechanical behavior of the cantilever; (b). optimization of the cantilever tip design according to the cantilever bending angle for the sake of larger electrical contact area with the bottom electrode (of the capacitor). Moreover, the current high transition temperatures of the Nitinol used are too high for biomedical implant application and hyperthermia treatment. This can be addressed by utilizing Nitinol material with lower transition temperatures close to the operation temperature in the hyperthermia treatment (40 - 45 °C). Moreover, the study on the thermal behavior of the circuit breaker integrated in the stent device in physiological saline flow will also be essential.

Bibliography

[1] G.A. Mensah GA and D.W. Brown DW, “An overview of cardiovascular disease burden in the United States,” *Health Aff (Millwood)*, vol. 26, no. 1, pp. 38–48, 200°.

[2] N. Townsend et al., “Cardiovascular disease in Europe: epidemiological update 2016,” *European Heart Journal*, vol. 37, no. 42, pp. 3232–3245, 2016.

[3] J. Cayton et al., “Current market trends of cardiac stents,” *Journal of Medical Marketing*, vol. 12, no.1, pp. 5-12, 2012.

[4] G. Dangas, V. Fuster, “Management of restenosis after coronary intervention,” *American Heart Journal*, vol. 132, no. 2, pp. 428-436, 1996.

[5] D. Buccheri, D. Piraino, G. Andolina, B. Cortese, “Understanding and managing in-stent restenosis: A review of clinical data, from pathogenesis to treatment,” *Journal of Thoracic Disease*, vol. 8, no. 10, pp. E1150-E1162, 2016.

[6] P.W. Serruys, M.J. Kutryk and A.T. Ong, “Coronary-artery stents,” *New England Journal of Medicine*, vol. 354, pp. 483-45, 2006.

[7] O.C. Marroquin, F. Selzer, S.R. Mulukutla et al, “A comparison of bare-metal and drug-eluting stents for off-label indications,” *New England Journal of Medicine*, vol. 368, no. 4, pp.342-352, 2008.

[8] M. I. Papafaklis, et al., “Drug-eluting stent restenosis: effect of drug type, release kinetics, hemodynamics and coating strategy," *Pharmacology & Therapeutics*, vol. 134, no. 1, pp. 43-53, 2012.

[9] F.G. Welt and C. Rogers, “Inflammation and restenosis in the stent era,” *Arteriosclerosis, Thrombosis, and Vascular Biology*, vo. 22, no. 11, pp. 1769–1776, 2002.

[10] M.A. Costa and D.I. Simon, “Molecular basis of restenosis and drug-eluting stents,” *Circulation*, vol. 111, no. 17, pp. 2257-2273, 2005.

[11] B. Ludewig, P. Krebs, E. Scandella, “Immunopathogenesis of atherosclerosis,” *Journal of Leukocyte*, vol. 76, no. 2, pp. 300-306, 2003.

[12] E. Hila et al., “Predicting in vivo efficacy of potential restenosis therapies by cell culture studies: species-dependent susceptibility of vascular smooth muscle cells,” *Open Cardiovasc Med J*, vol. 2, pp. 60-69, 2008.

[13] C. Bauters and J.M. Isner, “The biology of restenosis,” *Progress in Cardiovascular Diseases*, vol. 40, no. 2, pp. 107-116, 1997.

[14] G. Tocci et al., “Blood pressure levels at the time of percutaneous coronary revascularization and risk of coronary in-stent restenosis,” *American Journal of Hypertension*, vol. 29, no. 4, pp. 509-518, 2016.

[15] José M. Atienza, et al. "The influence of pressure and temperature on the behavior of the human aorta and carotid arteries." *Revista Española De Cardiología*, vol .60, no. 3, pp. 259-267, 2007.

[16] G. Baronzio, G. Parmar, M. Ballerini M, et al. “A brief overview of hyperthermia in cancer treatment,” *OMICS A: Journal of Integrative Biology*, vol. 3, no. 4, pp.115-125, 2014.

[17] A. Chicheł, J. Skowronek, M. Kubaszewska, M. Kanikowski, “Hyperthermia-Description of a Method and a Review of Clinical Applications,” *Reports on Practical Oncology and Radiotherapy*, vol. 12, no.5, pp. 267-275, 2007.

[18] K. Orihara, et al., “Hyperthermia at 43°C for 2 h inhibits the proliferation of vascular smooth muscle cells, but not endothelial cells,” *Journal of Molecular and Cellular Cardiology*, vol. 34, no. 9, pp. 1205-1215, 2002.

[19] C. Brasselet, et al., “Effect of local heating on restenosis and in-stent neointimal hyperplasia in the atherosclerotic rabbit model: A dose-ranging study,” *European Heart Journal*, vol. 29, no. 3, pp. 402-412, 2008.

[20] M.G. Floren, R.W. Günther, T. Schmitz-Rode, “Noninvasive Inductive Stent Heating: Alternative Approach to Prevent Instent Restenosis,” *Investigative Radiology*, vol. 39, no. 5, pp. 264-270, 2004.

[21] Y. Luo, M. Dahmardeh, X. Chen, K. Takahata, “A resonant-heating stent for wireless endohyperthermia treatment of restenosis,” *Sensors and Actuators A: Physical*, vol. 236, pp.323-333, 2015.

[22] K. Tanaka, et al., “A new radiofrequency thermal balloon catheter for pulmonary vein isolation,” *Journal of the American College of Cardiology*, vol. 38, no. 7, pp. 2079-2086, 2001.

[23] C.J. Li, Y.F. Zheng, L.C. Zhao, “Heating NiTi Stent in Magnetic Fields and the Thermal Effect on Smooth Muscle Cells,” *Key Engineering Materials*, vol. 288, pp. 579-582, 2005.

[24] A.B. Levitt, K. Robinson, N.A.F. Chronos, W. Daum, “External heating of stents by radio waves: Pilot studies in rabbit aorta,” *Cardiovascular Radiation Medicine*, vol. 4, no. 3, pp.133-138, 2003.

[25] D.B. Fram, et al. “In vivo radiofrequency thermal balloon angioplasty of porcine coronary arteries: histologic effects and safety.” *American Heart Journal*, vol. 126, no.4, pp.969-978, 1993.

[26] L. Li et al. “In vitro study on the feasibility of magnetic stent hyperthermia for the treatment of cardiovascular restenosis.” *Experimental and Therapeutic Medicine*, vol.6, no.2, pp. 347-354, 2013.

[27] Y. Luo, M. Dahmardeh, K. Takahata, "Biocompatible Circuit-Breaker Chip for Thermal Management of Biomedical Microsystems," *Journal of Micromechanics and Microengineering*, vol. 25, no. 5, pp. 055002, 2015.

[28] Y. Luo, X. Chen, M. Dahmardeh, K. Takahata, “RF-Powered Stent with Integrated Circuit Breaker for Safeguarded Wireless Hyperthermia Treatment,” *Journal of Microelectromechanical System*, vol. 24, no.5, pp.1293-1302, 2015.

[29] E. M. Yeatman, “Design and performance analysis of thermally actuated MEMS circuit breakers,” *Journal of Micromechanics and Microengineering*, vol. 15, pp. S109-S115, 2005.

[30] S. Kedia, and W. Wang, “Simulation, Design, Fabrication, and Testing of a MEMS Resettable Circuit Breaker,” *Journal of Microelectromechanical Systems*, vol. 24, no. 1, pp. 232-240, 2015.

[31] M.S. Mohamed Ali and K. Takahata, “Frequency-controlled wireless shape-memory-alloy microactuators integrated using an electroplating bonding process,” *Sensors and Actuators A: Physical*, vol. 163, no.1, pp. 363-372, 2010.

[32] J. Dvořák, et al., “Endovascular brachytherapy potentiated by hyperthermia in the prevention of vascular restenosis: A case report,” *Cardiovascular Radiation Medicine*, vol. 2, no. 4, pp. 205-207, 2001.

[33] K. Mahmoudi, A. Bouras, D. Bozec, R. Ivkov, C. Hadjipanayis, “Magnetic hyperthermia therapy for the treatment of glioblastoma: a review of the therapy’s history, efficacy and application in humans,” *International Journal of Hyperthermia*, vol. 34, no. 8, pp. 1316-1328, 2018.

[34] A.R. Mohammadi, M.S. Mohamed Ali, D. Lappin, C. Schlosser, K. Takahata, “Inductive antenna stent: Design, fabrication and characterization,” *Journal of Micromechanics Microengineering*, vol. 23, no. 2, pp. 025015:1-9, 2013.

[35] D. De Zutter, L. Knockaert, “Skin effect modeling based on a differential surface admittance operator,” *IEEE Transactions on Microwave Theory and Techniques*, vol. 53, no. 8, pp. 2526–2538, 2005.

[36] X. Chen, D. Brox, B. Assadsangabi, Y. Hsiang, K. Takahata, “Intelligent telemetric stent for wireless monitoring of intravascular pressure and its in vivo testing,” *Biomedical Microdevices*, vol. 16, no. 5, pp. 745–759, 2014.

[37] J. M. Osepchuk, and R. C. Petersen, “Safety standards for exposure to RF electromagnetic fields,” *IEEE Microwave Magazine*, vol. 2, no. 2, pp. 57-69, 2001.

[38] P. S. Rahko, “Evaluation of the Skin-To-Heart Distance in the Standing Adult by Two-Dimensional Echocardiography,” *Journal of the American Society of Echocardiography*, vol. 21, no. 6, pp. 761-764, 2008.

[39] C. Hassler, T. Boretius, T. Stieglitz, “Polymers for neural implants,” *Journal of Polymer Science Part B: Polymer Physics*, vol. 49, no. 1, pp. 18-33, 2011.

[40] Y. Yi, U. Buttner, Y. Fan, I.G. Foulds, “Design and optimization of a 3-coil resonance-based wireless power transfer system for biomedical implants,” *International Journal of Circuit Theory and Applications*, vol. 43, no.10, pp.1379-1390, 2015.

[41] Y. Yi, J. Kosel, “A remotely operated drug delivery system with dose control,” *Sensors and Actuators A: Physical*, vol. 261, pp. 177-183, 2017.

[42] H. Zafar, F. Sharif, M.J. Leahy, “Measurement of the blood flow rate and velocity in coronary artery stenosis using intracoronary frequency domain optical coherence tomography: Validation against fractional flow reserve,” *IJC Heart & Vasculature*, vol. 5, pp. 68-71, 2014.

[43] T. Duerig, A. Pelton, D. Stöckel, “An overview of nitinol medical applications,” *Materials Science and Engineering A*, vol. A273-275, pp. 149-160, 1999.

[44] S.W. Robertson, A.R. Pelton, R.O. Ritchie, "Mechanical fatigue and fracture of Nitinol," *International Materials Reviews*, vol. 57, no. 1, pp. 1-37, 2012.

[45] K. Takahata, "Micro-electro-discharge machining technologies for MEMS," *Micro Electronic and Mechanical Systems*, IntechOpen, 2009.

[46]. M.A. George, W.S. Glaunsinger, T. Thundat, S.M. Lindsay, "Electrical, spectroscopic, and morphological investigation of chromium diffusion through gold films." *Thin Solid Films*, vol. 189, pp.59-72, 1990.

[47] R. Audino, et al. "Interface behavior evaluation in gold/chromium, gold/titanium and gold/palladium/titanium thin films by means of resistivity and stylus measurements." *Thin Solid Films,* vol. 36, pp. 343-347, 1976.

[48] K.D. Kang, et al. "A Cr—Ag—Au metalization system." *IEEE Transactions on Electron Devices*, vol.16, pp. 356-360, 1969.

[49] D.L. Cocke et al. "The low-temperature thermal oxidation of copper, Cu_3O_2, and its influence on past and future studies." *Vacuum,* vol. 79, no. 1, pp. 71-83, 2005.

[50]. S. Siau, A. Vervaet, L. Degrendele, J.D. Baets, A.V. Calster, "Qualitative electroless Ni/Au plating considerations for the solder mask on top of sequential build-up layers*,"* *Applied Surface Science*, vol. 258, no. 8, pp. 2717-2740, 2006.

[51] S. Gao, Z. Chen, A. Hu, M. Li, K. Qian, "Electrodeposited Ni microcones with a thin Au film bonded with Au wire," *Journal of Materials Processing Technology*, vol. 2144, no.2, pp. 326–333, 2014.

[52]. M. Müller, and P. Valášek, "Influence of Environment Temperature on Strength of Quick-Setting Adhesives Based on Cyanoacrylates," *Advanced Materials Research*, vol. 4, pp. 1030-1032, 2014.

[53]. N. G. Senchenya, T. I. Guseva, and Yu. G. Gololobov, “Cyanoacrylate-based Adhesives,” *Polymer Science Series C*, vol. 49, no. 3, pp. 235–239, 2007.

[54]. D. Alaier, D. Baskaran, and M. Dadmun, “The influence of temperature on the polymerization of ethyl-cyanoacrylate from the vapor phase, ” *Reactive & Functional Polymers*, vol. 71, pp. 809-819, 2011.